

RESEARCH ARTICLE

10.1002/2015JF003718

Key Points:

- quantify landslide-channel connection for landslides triggered by the 2008 Wenchuan earthquake
- Identify topographic, lithologic and seismic controls on landslide-channel connection
- evaluate landslide location controls on post-seismic suspended sediment transport

Supporting Information:

- Supporting Information S1

Correspondence to:

G. Li,
genli@usc.edu

Citation:

Li, G., A. J. West, A. L. Densmore, D. E. Hammond, Z. Jin, F. Zhang, J. Wang, and R. G. Hilton (2016), Connectivity of earthquake-triggered landslides with the fluvial network: Implications for landslide sediment transport after the 2008 Wenchuan earthquake, *J. Geophys. Res. Earth Surf.*, 121, doi:10.1002/2015JF003718.

Received 31 AUG 2015

Accepted 26 MAR 2016

Accepted article online 1 APR 2016

Connectivity of earthquake-triggered landslides with the fluvial network: Implications for landslide sediment transport after the 2008 Wenchuan earthquake

Gen Li¹, A. Joshua West¹, Alexander L. Densmore², Douglas E. Hammond¹, Zhangdong Jin³, Fei Zhang³, Jin Wang³, and Robert G. Hilton²

¹Department of Earth Sciences, University of Southern California, Los Angeles, California, USA, ²Institute of Hazard, Risk and Resilience and Department of Geography, Durham University, Durham, UK, ³State Key Laboratory of Loess and Quaternary Geology, Institute of Earth Environment, Chinese Academy of Sciences, Xi'an, China

Abstract Evaluating the influence of earthquakes on erosion, landscape evolution, and sediment-related hazards requires understanding fluvial transport of material liberated in earthquake-triggered landslides. The location of landslides relative to river channels is expected to play an important role in postearthquake sediment dynamics. In this study, we assess the position of landslides triggered by the M_w 7.9 Wenchuan earthquake, aiming to understand the relationship between landslides and the fluvial network of the steep Longmen Shan mountain range. Combining a landslide inventory map and geomorphic analysis, we quantify landslide-channel connectivity in terms of the number of landslides, landslide area, and landslide volume estimated from scaling relationships. We observe a strong spatial variability in landslide-channel connectivity, with volumetric connectivity (ζ) ranging from ~20% to ~90% for different catchments. This variability is linked to topographic effects that set local channel densities, seismic effects (including seismogenic faulting) that regulate landslide size, and substrate effects that may influence both channelization and landslide size. Altogether, we estimate that the volume of landslides connected to channels comprises 43 + 9/–7% of the total coseismic landslide volume. Following the Wenchuan earthquake, fine-grained (<~0.25 mm) suspended sediment yield across the Longmen Shan catchments is positively correlated to catchment-wide landslide density, but this correlation is statistically indistinguishable whether or not connectivity is considered. The weaker-than-expected influence of connectivity on suspended sediment yield may be related to mobilization of fine-grained landslide material that resides in hillslope domains, i.e., not directly connected to river channels. In contrast, transport of the coarser fraction (which makes up >90% of the total landslide volume) may be more significantly affected by landslide locations.

1. Introduction

High-magnitude earthquakes can cause widespread landslides that collectively generate large volumes of clastic sediment [Keefer, 1984, 1994], contributing significantly to erosion in tectonically active mountain ranges [Dadson *et al.*, 2004; Korup *et al.*, 2004; Malamud *et al.*, 2004; Yanites *et al.*, 2010; Wang *et al.*, 2015]. Fluvial evacuation of landslide-derived sediment removes mass from mountains, influencing landscape evolution [Pearce and Watson, 1986; Malamud *et al.*, 2004; Korup *et al.*, 2007; Hovius *et al.*, 2011; Parker *et al.*, 2011; Egholm *et al.*, 2013; Li *et al.*, 2014]. Landslides also impact the terrestrial biosphere [Garwood *et al.*, 1979; Allen *et al.*, 1999; Clark *et al.*, 2016], and delivery of eroded material to river channels can redistribute essential nutrient elements (e.g., carbon and nitrogen), contributing to tectonic forcing of global biogeochemical cycles [Hilton *et al.*, 2011; Ramos Scharrón *et al.*, 2012; Jin *et al.*, 2016]. Furthermore, sediment supply from landslides to rivers may cause prolonged secondary natural hazards, via channel aggradation and enhanced flooding, and may reduce the storage capacity of downstream reservoirs [Korup *et al.*, 2004; Glade and Crozier, 2005; Huang and Fan, 2013; Wang *et al.*, 2015].

Several studies have quantified sediment mass flux and the associated residence times of landslide material in mountain belts using hydrological gauging data [Pearce and Watson, 1986; Dadson *et al.*, 2004; Korup *et al.*, 2004; Hovius *et al.*, 2011; Tsai *et al.*, 2013; Wang *et al.*, 2015], topographic surveys of individual rivers [Liu *et al.*, 2015; Yanites *et al.*, 2010], and geochemical measurements such as cosmogenic nuclide inventories [West *et al.*, 2014; McPhillips *et al.*, 2014]. Other studies have used numerical models to predict the entrainment,

transport, and deposition of sediment and to predict evacuation rates [e.g., *Attal and Lavé, 2006; Cui et al., 2003; Sutherland et al., 2002; Ferguson et al., 2015*]. All of these approaches depend on understanding the amount of sediment that landslides make available for fluvial transport, which is determined by the number and size of landslides as well as by their location. Earthquake-triggered landslides are not distributed evenly across landscapes: some are directly connected to river channels and thus prone to fluvial transport, whereas others are sequestered on hillslopes away from the river network, where they are expected to contribute less immediately to the riverine sediment budget [*Meunier et al., 2008; Dadson et al., 2004; Hovius et al., 2011; Huang and Fan, 2013*]. Moreover, earthquake-triggered landslides have a range of sizes [*Malamud et al., 2004*], potentially affecting their impact on river systems. The “landslide-landscape relationship” [*Dadson et al., 2004; Hovius et al., 2011; Tsai et al., 2013*], which is governed by factors such as the hydrological and topographic characteristics of the landscape, the location of landslides, and the geometric properties (e.g., size and runout length) of landslides, is expected to determine the magnitude and duration of associated sediment transport. But key aspects of this relationship and how it controls sediment dynamics are not completely understood.

Previous studies of landslide spatial distribution have measured landslide locations with respect to channels versus ridges, demonstrating that landslides cluster in specific landscape positions depending on hillslope topography and the landslide triggering mechanism, e.g., earthquake versus rainstorm [*Densmore and Hovius, 2000; Meunier et al., 2008; Huang and Montgomery, 2014*]. Other studies have distinguished landslides that are “visibly connected” to river channels and presumably available for fluvial transport [*Hilton et al., 2011; West et al., 2011; Clark et al., 2016*]. For the 1999 M_w 7.6 Chi-Chi earthquake in Taiwan, an estimated 8% of the earthquake-triggered landslide population was connected to channels [*Dadson et al., 2004*], and this connectivity showed little spatial variability [*Hovius et al., 2011*]. The 2008 M_w 7.9 Wenchuan earthquake and associated widespread landsliding in China provide an opportunity to explore systematically how and why landslide-landscape relationships vary spatially and to assess how this variability might regulate sediment export.

In this paper, we characterize the spatial distribution of coseismic landslides associated with the Wenchuan earthquake, allowing us to evaluate the extent to which landslide debris is delivered directly to channels, and we then explore how this distribution affects postearthquake sediment export by rivers. We map hillslope and channel domains using a digital elevation model of the regional topography, and we identify landslide populations in each setting using a coseismic landslide inventory. We define and quantify landslide-channel volumetric connectivity (ξ) for the Wenchuan landslide inventory and use a new catchment-averaged metric, the landslide location index (ψ), as a reference for comparison to our calculation of ξ . We find that landslide-channel connectivity varies across the Longmen Shan region, and we investigate the effects of seismology, topography, and geology on the spatial variability of ξ , providing general insight into the factors that determine connectivity between landslides and river channels. Finally, we assess the role that landslide-channel connectivity may play in determining river sediment yields in the years following the earthquake.

2. Setting

2.1. Topography, Hydrology, and Climate

The Longmen Shan mountain range defines the eastern margin of the Tibetan Plateau and marks the steepest topographic gradient among modern-day plateau edges [*Burchfiel et al., 1995; Densmore et al., 2007a*] (Figure 1a). This region is characterized by a steep, high-relief margin on the east, with > 5 km elevation rise over 50 km horizontal distance from the Sichuan Basin [*Burchfiel et al., 2008*]. Relief decreases westward toward the Tibetan Plateau (Figures 2b–2d). Several large rivers, including the Min Jiang, Tuo Jiang, Fu Jiang, Jialing Jiang, Qingyi Jiang, and Dadu He, drain the Longmen Shan range. River suspended sediment flux data indicate a denudation rate of ~ 0.5 mm/yr during the decades before the 1990s [*Liu-Zeng et al., 2011*], comparable to ^{10}Be -derived millennial denudation rates and geological exhumation rates [*Liu-Zeng et al., 2011; Godard et al., 2010; Ouimet et al., 2009*]. The regional climate is dominated by the East Asian monsoon, with average annual rainfall varying from ~ 1100 mm at the margin to ~ 600 mm on the plateau. About 70%–80% of the precipitation occurs from June to September [*Liu-Zeng et al., 2011*].

2.2. Geology

The bedrock geology of the Longmen Shan is dominated by a Proterozoic basement of granitoid and high-grade metamorphic rocks, a Paleozoic passive margin sequence of metasediments and granitic intrusions, and a thick Mesozoic foreland basin succession composed of marine and clastic sediments [*Burchfiel et al.,*

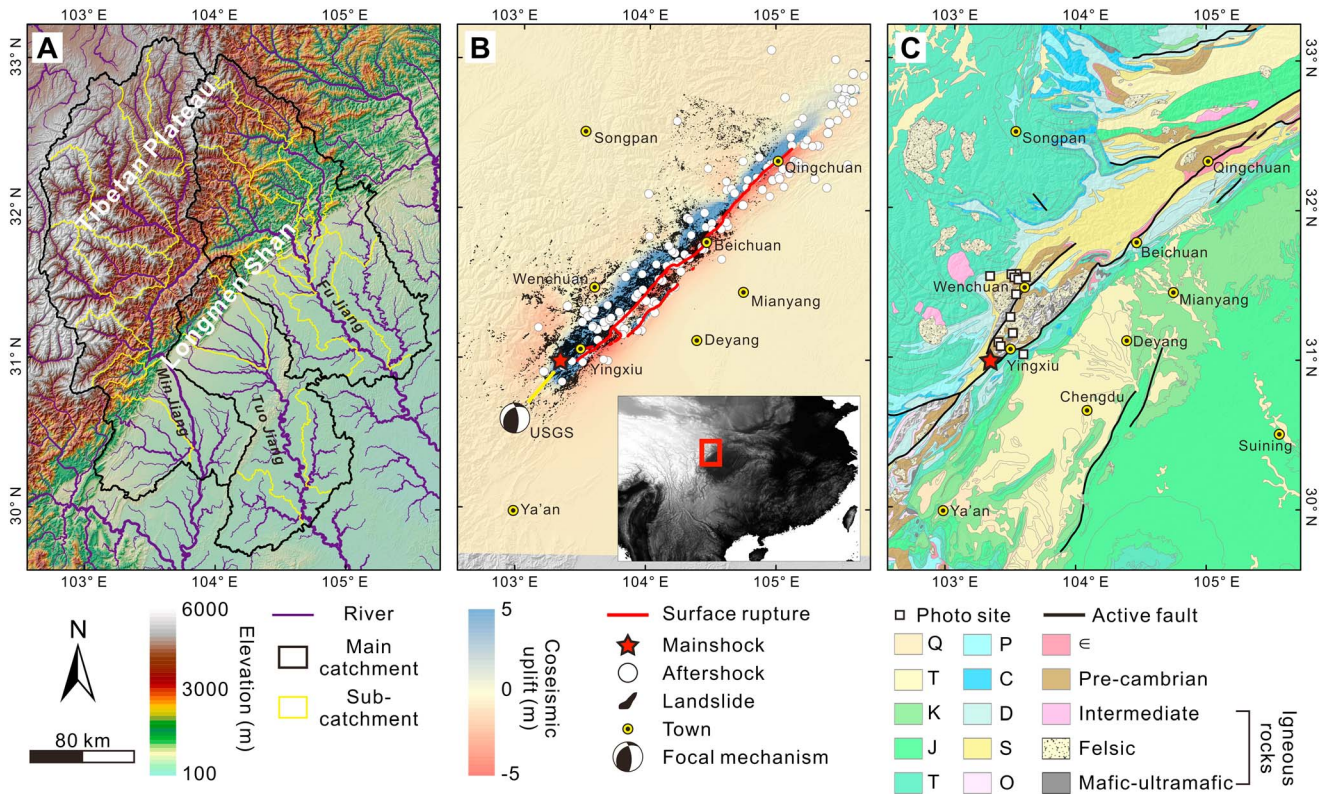


Figure 1. Maps of the Longmen Shan region of the eastern Tibetan Plateau and adjacent Sichuan Basin. (a) Shaded relief map (from SRTM-derived DEM) of the study area with the three large river catchments (Min Jiang, Tuo Jiang, and Fu Jiang) outlined in black. (b) Major lithological units and faults of the eastern Tibetan Plateau region, including mainly Proterozoic (pE) granitoids and high-grade metamorphic rocks, Paleozoic (including E: Cambrian, O: Ordovician, S: Silurian, D: Devonian, C: Carboniferous, and P: Permian), and Mesozoic (including T: Triassic, J: Jurassic, and K: Cretaceous) passive margin and foreland basin sequences, and limited Cenozoic (including Q: Quaternary) sediment, modified from a 1: 2,500,000 China Geological Base Map [China Geological Survey, 2004]. (c) Epicenter, focal mechanism, after-shocks, PGA contours [USGS Earthquake Hazard Program, 2008], surface deformation [Fielding et al., 2013], coseismic landslides [Li et al., 2014], and fault rupture associated with the 2008 M_w 7.9 Wenchuan earthquake [Liu-Zeng et al., 2009].

1995; Li et al., 2003; Densmore et al., 2007a] (Figure 1b). Three large faults, the Wenchuan-Maowen fault, the Yingxiu-Beichuan fault, and the Pengguan fault, all strike parallel to the Longmen Shan margin (Figure 1b). These faults were reactivated in the India-Asia collision and have been active as dextral-thrust oblique-slip faults during the late Cenozoic [Burchfiel et al., 1995; Densmore et al., 2007a; Wang and Meng, 2009]. Before 2008, GPS measurements showed slow deformation rates across the Longmen Shan range, implying limited strain accumulation and low perceived seismic hazard [Zhang et al., 2004; Meade, 2007; Kirby et al., 2008]. The recurrence time for large, catastrophic earthquakes like the 2008 Wenchuan event in the Longmen Shan range is estimated to be ~2000–4000 years based on geodetic and paleoseismic observations [Densmore et al., 2007a; Shen et al., 2009].

2.3. Seismology and Landsliding

The M_w 7.9 Wenchuan earthquake occurred on 12 May 2008. Rupture initiated in the southern Longmen Shan and propagated for ~270 km along segments of the Yingxiu-Beichuan and Pengguan faults (Figure 1c) [Burchfiel et al., 2008; Shen et al., 2009]. Fault displacements and seismic moment release varied along the rupture trace but were highest around Yingxiu and Beichuan [Xu et al., 2009; Shen et al., 2009; Liu-Zeng et al., 2009]. The motion along the fault changed from predominantly thrusting in the southwest, near the epicenter, to strike slip in the northeast [Shen et al., 2009; Xu et al., 2009]. The strong ground motion and intensive seismic shaking caused over 60,000 coseismic and immediately postearthquake (defined here as occurring within 6 months) landslides (Figure 1c) [Dai et al., 2011; Parker et al., 2011; Li et al., 2014]. Large increases in sediment fluxes have been observed after the earthquake from hydrometric gauging of rivers [Wang et al., 2015] and ^{10}Be measurements on detrital quartz from riverbed sediments [West et al., 2014]. These methods both average over the spatial scale of river catchments that span areas > 1000 km² and include thousands of landslides.

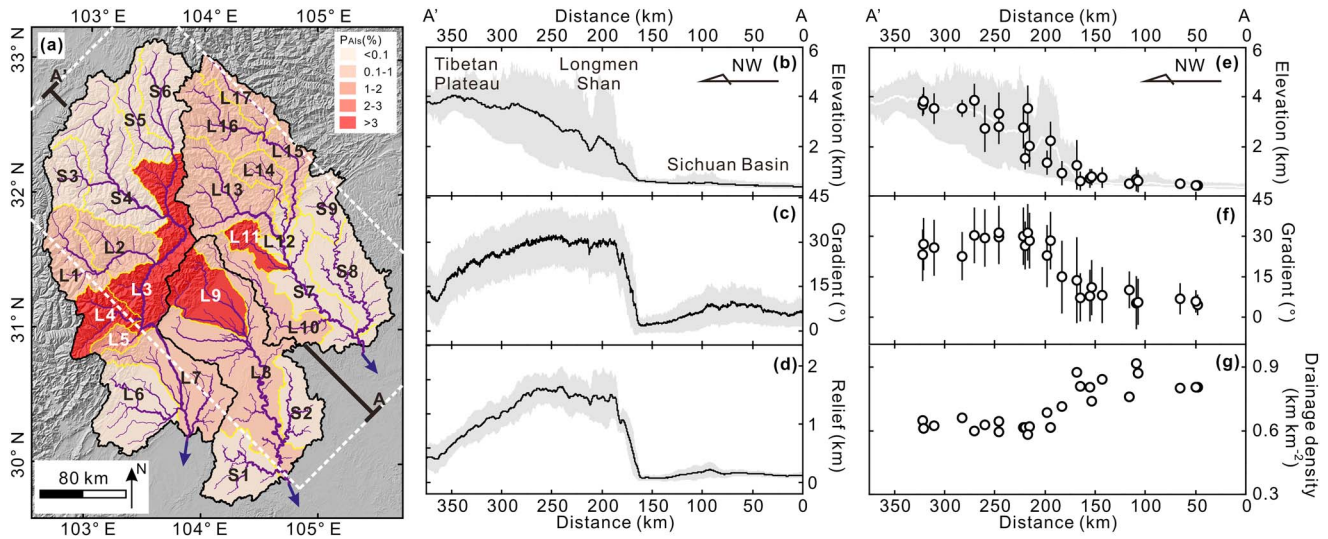


Figure 2. Hydrological map and geomorphic swath profiles of the study area. (a) The fluvial network in the study area with basins color coded by areal landslide density P_{AIs} . Yellow lines show the boundaries of subcatchments and tributaries, and black lines show the boundaries of the three main catchments (Min Jiang, Fu Jiang, and Tuo Jiang). Color shading represents landslide areal density in each subcatchment and tributary, with 17 catchments defined as having significant landslide impact (L1–L17, Table 2) and the remaining (S1–S9) as having negligible landslide impact. A–A' represents the trend of 170 km-wide swath profiles (bounded by white dashed lines) along the steepest topographic gradient shown in Figures 2b–2g. (b) Profile of elevations in the study area, showing maximum, mean, and minimum elevations. (c) Profile of topographic gradients in the study area, showing mean gradient and the range (grey area) bounded by 1 standard deviation. (d) Profile of relief in the study area, showing mean relief calculated with a 2.5 km radius circular window (black line) and the range (grey area) bounded by 1 standard deviation. Figures 2e–2g are plotted by projecting the calculated parameters for subcatchments to the trend line A–A' (Figures 2e–2g). (e) Mean elevations for subcatchments and tributaries, with shaded background showing the mean, maximum, and minimum elevations in the study area; error bars indicate the 1σ range of elevations in each subcatchment. (f) Mean gradients for subcatchments and tributaries, with error bars representing 1σ range. (g) Channel densities for subcatchments and tributaries. Fluvial channel densities are higher ($\sim 0.9 \text{ km km}^{-2}$) on the eastern flank of the Longmen Shan and the Sichuan Basin and lower ($\sim 0.6 \text{ km km}^{-2}$) toward the Tibetan Plateau.

3. Materials and Approach

3.1. Landslide Inventory Mapping and Volume Estimation

Li *et al.* [2014] produced a coseismic and immediately postearthquake landslide inventory map (Figure 1c) using high-resolution images collected within 6 months of the Wenchuan earthquake from SPOT and DigitalGlobe satellites. Postearthquake images were compared with those collected before the earthquake. The mapping technique combined automated algorithms and manual screening, allowing removal of nonlandslide objects and segmentation of amalgamated landslides, which can significantly bias volume estimates [Li *et al.*, 2014; Marc and Hovius, 2015]. Landslides were mapped at 10 m spatial resolution. At this resolution, it was not possible to separate depletion zones (i.e., landslide scars) versus accumulation zones (i.e., deposits), so mapped landslide polygons include both scars and deposits. For this study, we have slightly expanded the mapped region reported previously [Li *et al.*, 2014], based on newly available imagery and using identical techniques (Figure 1c).

Landslide volumes were calculated using empirical area-volume scaling relationships [Guzzetti *et al.*, 2009; Larsen *et al.*, 2010; Yanites *et al.*, 2010; Parker *et al.*, 2011; Li *et al.*, 2014]:

$$V_{Is}^i = \alpha(A_{Is}^i)^\gamma \tag{1}$$

and

$$V_{Is} = \sum_i \alpha(A_{Is}^i)^\gamma \tag{2}$$

where A_{Is}^i and V_{Is}^i are the area and the volume for one single landslide, respectively, V_{Is} is the total landslide volume, and α and γ are empirical scaling factors (A list of used symbols is reported in Table 1). The scaling factors α and γ and related uncertainties were determined in the Longmen Shan based on field measurements of the depths of landslide scars (see supporting information for details) [e.g., Parker *et al.*, 2011; Whadcoat, 2011]. Uncertainties reported with the original publication of landslide volumes included propagation of uncertainty on the scaling parameters [Li *et al.*, 2014] but did not account for additional uncertainty

Table 1. Notation for Symbols

Symbol	Notation	Unit	Equation
			Introduced
A_{Is}	Landslide area	km^2 or m^2	1
V_{Is}	Landslide volume	km^3 or m^3	1
γ	Landslide area-volume scaling factor, $\gamma = 1.388 \pm 0.087$ [Li et al., 2014]	$\text{m}^{(3-2\alpha)}$	1
α	Landslide area-volume scaling factor, $\text{Log}_{10} \alpha = -0.974 \pm 0.366$ [Li et al., 2014]	Dimensionless	1
A	Upstream contributing area	km^2	3
P_{AIs}	Landslide areal density	%	3
P_{VIs}	Landslide volumetric density	$\text{m}^3 \text{km}^{-2}$	4
L	Channel length	km	5
ρ	Drainage density	km km^{-2}	5
ψ	Landslide location index	Dimensionless	6
IA_c	Integrated area for catchment landscapes on distribution plots for A	Dimensionless	6
IA_{Is}	Integrated area for landslides on distribution plots for A	Dimensionless	6
m	Inverse-gamma function parameter	m^2	7
s	Inverse-gamma function parameter	m^2	7
q	Inverse-gamma function parameter	Dimensionless	7
G	Gradient	$^\circ$ or m m^{-1}	
ζ	Landslide-channel volumetric connectivity	%	
PGA	Peak ground acceleration	g	

resulting from applying area-volume calibrations defined principally by scar areas to mapped landslide areas that include both scars and deposits [Cruden and Varnes, 1996]. To constrain this additional uncertainty, we used high-resolution (0.5 m) WorldView images, which allowed identification of scars and deposits. We estimated scar area as a proportion of total landslide area for >500 landslides. Using this subset of landslides, we find that our mapping approach that does not distinguish scars versus deposits may overestimate landslide areas by ~15–30%, depending on assumptions about the proportion of scar areas covered by landslide deposits (see supporting information). This uncertainty is much smaller than the ~+260%/–70% uncertainty arising from the scaling parameters alone [Li et al., 2014]. Since we lack imagery at sufficiently high resolution to distinguish scars from deposits across the entire Wenchuan study area, in this study we use the uncertainties from scaling factors, consistent with Li et al. [2014], acknowledging that the definition of landslide areas introduces a minor additional bias. We note that distinguishing scars from deposits and carefully considering what areas have been used in calibration data sets [e.g., Larsen et al., 2010] would help reduce uncertainties on volume estimates in future landslide studies.

We have considered only coseismic and immediately postearthquake landslides in this study. Observations of enhanced postseismic landslide rates have been attributed to rock weakening during shaking [Dadson et al., 2004; Marc et al., 2015], and postseismic landslides may deliver additional sediment to river systems [Dadson et al., 2004; Hovius et al., 2011]. However, following earthquakes in Taiwan, Japan, and Papua New Guinea, postseismic landslides added only a very small proportion (~2–5%) to the volume of coseismic landslides [Marc et al., 2015]. For the Wenchuan case, local studies (catchments covering < 4% of the total landslide-impacted area) show that rainfall-triggered, postseismic landslides added 51% to the landslide number, 30% to the landslide area, and ~20% to the coseismic landslide volume (volumetric addition estimated based on equations (1) and (2)) in 2008, and 5% to the landslide volume in 2010 [Tang et al., 2011; Zhang et al., 2014]. The areas covered in these studies are in the frontal Longmen Shan, with the most favorable conditions for postseismic landsliding (proximity to the faults, highest coseismic shaking, and most intense rainfall). For the whole Longmen Shan, we expect postseismic landsliding following the Wenchuan earthquake to be relatively less important, perhaps more analogous to the Chi-Chi case in Taiwan [Marc et al., 2015]. Further work mapping post-Wenchuan landslides would be needed to better constrain these values, but we do not expect these additional landslides to significantly change the results and conclusions of this study.

3.2. Topographic and Hydrographic Mapping

For topographic analysis, we used 87 m resolution postprocessed SRTM data from the Consultative Group for International Agricultural Research that includes regional void filling using other data products (local data sources and SRTM 30 data) and reinterpolation algorithms [Jarvis et al., 2008]. We expect that the digital

elevation model (DEM) data provide meaningful information about landslide locations in the study area, since regional hillslope length scales are around 1 km [Kirby *et al.*, 2003]. This length is equivalent to >10 DEM cells, sufficient to define hillslope and channel morphology. We calculated topographic gradient (G) and upstream contributing area (A) for each DEM raster cell using the Spatial Analyst toolbox in ArcGIS software package. Although calculated gradients are strongly dependent on DEM resolution [e.g., Larsen *et al.*, 2014], the biases are systematic and the relative trends between different sites should not be influenced. Since we are most interested in the relative values of gradients and general patterns in this study, we used uncorrected values derived from the SRTM DEM.

To map hydrographic networks, we used a geographic data set of ordered catchments and drainage basins from the Chinese Lake and Watershed Data Center [http://lake.geodata.cn/]. We focused on the three main large river catchments draining the Longmen Shan: the Min Jiang, Tuo Jiang, and Fu Jiang, which together cover ~90% of the total area affected by Wenchuan coseismic landslides. We mapped 26 subcatchments and tributary catchments with reference to the geographic data set (Figure 2a). Subcatchments were defined as constituent segments of a main catchment along the main stem (for example, Min Jiang Pengshan-Dujiangyan segment, catchment L7 in Figure 2a), and tributary catchments were defined as those secondary catchments contributing to a main stem (for example, the Yuzixi catchment, catchment L4 in Figure 2a). All the catchments were analyzed independently. Parts of the studied catchments are monitored by the hydrological gauging network of the Chinese Bureau of Hydrology [Wang *et al.*, 2015] (Table 2).

Using the landslide inventory map, we quantified landslide impact by calculating the landslide areal density P_{AIs} (%) for each catchment:

$$P_{AIs} = \frac{A_{Is}}{A} \times 100\% \quad (3)$$

where A is the area of a selected catchment and A_{Is} is the total area of landslides in the catchment. Seventeen of the 26 tributary and subcatchments had substantial landslide impacts, with P_{AIs} ranging from 0.1% to 5% (catchments L1–L17, Figure 2a and Table 2). Similarly, we also defined the landslide volumetric density P_{VIs} ($\text{m}^3 \text{km}^{-2}$) for each catchment:

$$P_{VIs} = \frac{V_{Is}}{A} \quad (4)$$

where V_{Is} is the total volume of landslides in the selected catchment.

Channels across the study area were derived from the DEM by using gradient-upstream area relations [Dadson *et al.*, 2004; Meunier *et al.*, 2008; Huang and Montgomery, 2014]. In this study, we specifically refer to “fluvial” channels, as distinct from “colluvial” channels and other types of hillslope areas upstream of the channel head, in order to characterize landslide distribution within the landscape. For each tributary and subcatchment, we plotted the G - A relationship for all raster cells (Figure 3) and defined fluvial channels based on the expected power law G - A relationship [e.g., Montgomery and Foufoula-Georgiou, 1993; Montgomery and Buffington, 1997; Sklar and Dietrich, 1998; Montgomery, 2001; Stock and Dietrich, 2003; Densmore *et al.*, 2007b] (e.g., Figure 3a). Specifically, we fit a group of linear relations to segments of the logarithmic G - A plots and identified five major geomorphic process domains: (1) hillslope, (2) valley head, (3) colluvial, (4) bedrock, and (5) alluvial [cf. Montgomery, 2001; Brardinoni and Hassan, 2006]. Modifying the “pruning” approach for determining power law fits on G - A plots [Stock and Dietrich, 2003; Densmore *et al.*, 2007b], we first calculated a linear fit on logarithmic G - A plots at the smallest upstream areas. We then successively added larger upstream areas and refit the linear relation until a local optimal fit was identified (based on correlation coefficient and mean squared residuals). Using this procedure, we identified domains with linear behavior and uniform power law exponent on logarithmic G - A plots. We repeated this approach, together with visual examination, to define successive domains with higher A values in the logarithmic G - A plots (e.g., progressing from hillslopes to valley heads to colluvial to bedrock and finally to alluvial domains). The A value defining the transition between the colluvial and bedrock domains (determined as the transition between domains (3) and (4) [cf. Montgomery, 2001]) was then selected as a threshold area, A_{\min} , to represent a minimum upstream area for channelization, thus distinguishing fluvial channels from hillslopes (Figure S3 L1–L17 in the supporting information) [Montgomery, 2001; Dadson *et al.*, 2004; Brardinoni and Hassan, 2006; Meunier *et al.*, 2008]. We found that most catchments yielded $A_{\min} \sim 1 \text{ km}^2$. Some catchments showed more scatter and less clear transitions among domains on the G - A plots (L6, L8, L10, and L12, see supporting information Figure S1), and

Table 2. Topographic and Landslide Parameters for the Catchments in the Study Area

Large catchment	ID	Catchment Name	Controlling Hydrological Station	Catchment Type	Area (km ²)	Elevation (Mean ± 1σ) (m)	Slope (Mean ± 1σ) (°)	Drainage Density (km ⁻¹)	<i>P_{ALS}</i> (%) ^a	Landslide-Channel Volumetric Connectivity ζ^b (%)	Landslide Location Index ψ^c
Min Jiang	L1	Upper Zagunao above Zagunao	Zagunao	Tributary	2397	3864 ± 634	30 ± 10	0.60	0.220	44 + 2/-3	1.49
	L2	Lower Zagunao above Sangping	Sangping	Tributary	2220	3350 ± 786	31 ± 10	0.60	0.351	21 + 2/-1	1.19
	L3	Min Jiang Dujiangyan to Zhenjiangguan	Dujiang	Subcatchment	4341	2780 ± 834	30 ± 10	0.61	5.184	29 + 1/-1	1.27
Fu Jiang	L4	Yuzixi	N.A. ^d	Tributary	1735	3546 ± 877	31 ± 10	0.58	3.395	34 + 2/-2	1.29
	L5	Guojiaba	Guojiaba	Tributary	575	2253 ± 713	28 ± 10	0.61	1.802	20 + 1/-1	1.15
	L7	Min Jiang Pengshan to Dujiangyan	Pengshan	Subcatchment	3980	690 ± 460	5 ± 10	0.92	0.209	45 + 9/-9	1.32
	S3	Upper Heishui He above Heishui	Heishui	Tributary	1716	3852 ± 527	27 ± 9	0.61	0.003	N.A. ^f	N.A. ^g
Tuo Jiang	S4	Lower Heishui He above Shaba	Shaba	Tributary	5484	3541 ± 592	26 ± 10	0.62	0.003	N.A. ^f	N.A. ^g
	S5	Xiaoxingou	N.A. ^d	Tributary	1700	3540 ± 313	23 ± 9	0.66	N.A. ^e	N.A. ^e	N.A. ^g
	S6	Min Jiang above Zhenjiangguan	Zhenjiangguan	Subcatchment	2770	3677 ± 394	23 ± 9	0.65	N.A. ^e	N.A. ^e	N.A. ^g
	L8	Tuo Jiang above Dengyingyan	Dengyingyan	Subcatchment	7321	607 ± 425	6 ± 8	0.87	0.411	58 + 9/-9	1.39
Fu Jiang	L9	Jian Jiang	N.A. ^d	Tributary	2859	1256 ± 988	14 ± 16	0.88	4.065	50 + 4/-5	1.29
	S1	Qixi He	N.A. ^d	Tributary	2497	428 ± 54	5 ± 4	0.81	<0.001	N.A. ^f	N.A. ^g
	S2	Zishui He	N.A. ^d	Tributary	1959	435 ± 30	6 ± 4	0.81	<0.001	N.A. ^f	N.A. ^g
	L6	Danan He	N.A. ^d	Tributary	3620	753 ± 401	8 ± 10	0.84	0.032	36 + 1/-2	1.24
	L10	Kai Jiang above Santai	Santai	Tributary	2560	611 ± 355	7 ± 9	0.81	0.764	91 + 4/-9	1.8
	L11	Anchang He	N.A. ^d	Tributary	957	935 ± 462	15 ± 13	0.71	3.846	34 + 3/-3	1.25
	L12	Fu Jiang Fujiangqiao to Jiangyou	Fujiangqiao	Subcatchment	707	723 ± 357	8 ± 9	0.81	0.094	16 + 1/-1	1.15
	L13	Tongkou He	N.A. ^d	Tributary	4217	2016 ± 825	28 ± 10	0.62	0.970	46 + 7/-7	1.33
	L14	Pingtong He above Ganxi	Ganxi	Tributary	1062	1526 ± 426	27 ± 9	0.62	0.135	17 + 1/-1	1.12
	L15	Fu Jiang Jiangyou to Pingwu	Jiangyou	Subcatchment	1581	1341 ± 464	23 ± 11	0.69	0.245	34 + 1/-1	1.19
	L16	Fu Jiang above Pingwu	Pingwu	Subcatchment	2808	2729 ± 932	29 ± 10	0.63	0.102	8 + 2/-2	1.19
	L17	Huoxi He	N.A. ^d	Tributary	1494	2815 ± 679	30 ± 10	0.64	0.150	23 + 2/-3	1.21
Fu Jiang	S7	Fu Jiang Shehong to Fujiangqiao	Shehong	Subcatchment	3088	480 ± 66	7 ± 6	0.80	N.A. ^e	N.A. ^e	N.A. ^g
	S8	Lower Zitong Jiang	N.A. ^d	Tributary	3505	503 ± 81	10 ± 6	0.76	N.A. ^e	N.A. ^e	N.A. ^g
	S9	Upper Zitong Jiang above Zitong	Zitong	Tributary	1546	770 ± 311	11 ± 10	0.74	N.A. ^e	N.A. ^e	N.A. ^g

^a*P_{ALS}* (%): landslide area density calculated as landslide area/catchment area (equation (3)).
^b ζ : landslide-channel volumetric connectivity; results are reported as the medians and the 5th and 95th percentiles from 1000 Monte Carlo simulations propagating uncertainties from landslide area-volume scaling.
^c ψ : catchment landslide location index, as calculated from equation (6) and Figure 4, see more details in supporting information.
^dNot available.
^eLandslide coverage is not available due to lack of satellite imagery coverage. These catchments are beyond the 0.2 g PGA contour [USGS Earthquake Hazard Program, 2008] (<http://earthquake.usgs.gov/earthquakes>) and have low relief, suggesting low landslide susceptibility.
^fLandslide-channel connectivity was not calculated for catchments with *P_{ALS}* < 0.01% and areas with no imagery coverage.
^gLandslide location index was not calculated for catchments with *P_{ALS}* < 0.01% and areas with no imagery coverage.

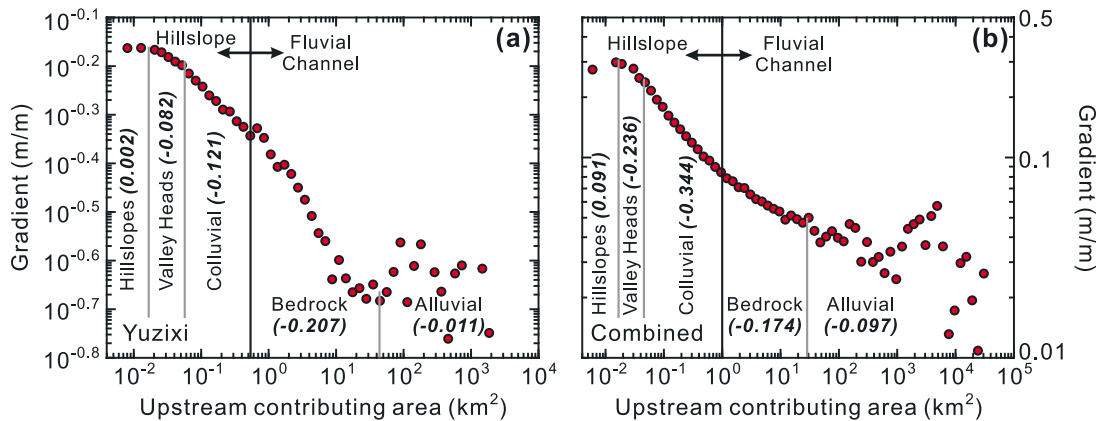


Figure 3. Gradient-upstream contributing area diagrams for the Yuzixi catchment (L4) and for the combined Longmen Shan catchments (compilation of L1–L17, Table 2). (a) Example of a logarithmic G - A diagram from the Yuzixi catchment, with characterization of domains dominated by different geomorphic processes following Montgomery [2001]. Mean gradients are calculated in each A bin ($\delta \log_{10} A = 0.1$), and the power law exponents between G and A (i.e., the slope of linear regression on logarithm plots) are reported for each landscape zone. In this and other similar studies [e.g., Dadson et al., 2004; Meunier et al., 2008], bedrock and alluvial areas are defined as the channel domain, and hillslope (strictly defined by the positive exponent on the G - A diagram), valley head, and colluvial areas are grouped together as the hillslope domain. (b) A logarithmic G - A diagram combining all Longmen Shan catchments (L1–L17, Table). The regional channel threshold of $A_{\min} \sim 1 \text{ km}^2$ is used for catchments where data are noisier, with less clear transitions than shown in these examples. G - A plots for all catchments are shown in the supporting information.

so for those catchments we used a regional channel threshold A_{\min} of 1 km^2 , as derived from the G - A relation combining all Longmen Shan catchments (Figure 3b).

Parts of catchments with $A > A_{\min}$ were defined broadly as channel domains (including alluvial-bedrock channels and alluvial channels), while parts with $A < A_{\min}$ were defined broadly as hillslope domains, including colluvial channels, valley heads, and strictly defined “hillslopes.” The latter are often characterized by a positive G - A exponent indicating convexity [Montgomery, 2001; Brardinoni and Hassan, 2006], but our general definition of hillslope as used in this analysis simply refers to those regions outside of the fluvial network, rather than regions with convex morphology per se.

To quantify the extent of fluvial channelization in each catchment, we calculated the drainage density (ρ , km km^{-2}) as

$$\rho = \frac{L}{A} \tag{5}$$

where L (km) is the total length of fluvial channels within the catchment [Dingman, 1978]. We observe a decline in drainage density from the basin toward the plateau (Figure 2g).

We plotted 170 km wide swath profiles (Figures 2b–2g) along the trend of the steepest topographic gradient (NW-SE, perpendicular to the Longmen Shan faults). We projected mean elevation, relief, gradient, and catchment-scale drainage density ρ onto the swath trend (A - A' in Figure 2). Catchment-scale relief was defined as the range of elevations within a 2.5 km radius circle [e.g., Montgomery and Brandon, 2002; DiBiase et al., 2010]. The same parameters for each subcatchment and tributary catchment were also projected onto the swath profile trend A - A' (Figures 2e–2g).

3.3. Characterizing Landslide Locations and Constraining Uncertainties

To determine the locations of landslides relative to the fluvial network, we compared the maximum upstream contributing area value within each mapped landslide polygon with the threshold A_{\min} for channels within that catchment. If the maximum A for a landslide was larger than A_{\min} , the entire landslide was assigned as connected to or located within the channel domain, while landslides with maximum A values smaller than A_{\min} were defined as located on hillslopes. This approach provides an algorithm for estimating whether the toe of a landslide intersects what we have classified as a channel [e.g., Dadson et al., 2004; Meunier et al., 2008; Huang and Montgomery, 2014]. We then calculated the proportions of all landslides that are connected to the river system in terms of numbers of landslides

(“population connectivity”), landslide area (“areal connectivity”), and landslide volume (“volumetric connectivity”). To determine volumetric connectivity, we combined the landslide geomorphic classification and the landslide area-volume scaling relation, using a Monte Carlo random sampling method to estimate uncertainties sourced from the landslide area-volume scaling parameters α and γ in equation (2). We determined the volumetric percentage of channel-connected landslides in the whole landslide inventory and for landslides within individual catchments; we term this percentage the landslide-channel volumetric connectivity, ξ (%), for each catchment [cf. *Dadson et al., 2004; Meunier et al., 2008; Hovius et al., 2011; Huang and Montgomery, 2014*].

Whereas the landslides were mapped at 10 m resolution, the DEM had a coarser resolution of ~ 87 m. The inconsistent resolutions between the landslide inventory and the DEM data set could introduce potential sampling bias: the actual upstream contributing area value of an individual landslide cell may not be the same as the A value of the larger DEM cell. To constrain the uncertainties that arise by extracting the landslide upstream area values from a coarser A raster, we estimated the potential difference between sampling a 10 m resolution raster data set and an 87 m resolution raster data set (details in supporting information). Our results show that the maximum sampling error on A is around 0.01 km^2 , on the order of 1% of the threshold upstream area for channels ($\sim 1 \text{ km}^2$), and that the maximum error decays quickly as A grows (see supporting information Figure S2). For comparison to this theoretically predicted uncertainty, we also considered the difference between calculations using 87 m versus 30 m SRTM data. We observed some spatial mismatch of channels extracted from these two DEMs in the same catchment, and these differences introduced $\sim 0.1 \text{ km}^2$ difference in calculated upstream areas (see supporting information). This difference is ~ 10 times higher than the predicted uncertainty arising from the difference in resolution alone, pointing to the importance of other factors such as voids and DEM accuracy. Our evaluation of connectivity is not strongly biased by this level of uncertainty, when considering the sensitivity of connectivity estimates to threshold values.

To evaluate the sensitivity of connectivity to channel threshold A_{min} , we calculated connectivity for each catchment across a wide range of A_{min} values as reported in the Longmen Shan and other mountain belts ($\sim 0.3\text{--}3 \text{ km}^2$) [*Kirby et al., 2003; Montgomery, 2001; Dadson et al., 2004; Meunier et al., 2008*] (supporting information Figure S3). We found that the connectivity determined using variable A_{min} differed by $\sim 20\%$ (relative percentage) when compared to using the catchment-specific A_{min} determined in this study (supporting information Figure S4), leading us to conclude that calculated connectivity is relatively insensitive to uncertainty in A_{min} .

3.4. Catchment-Scale Landslide Location Index

To complement the gradient-upstream area approach, we propose a new metric that considers landslide locations at the catchment scale. The “landslide location index” (ψ , dimensionless) for individual catchments characterizes how landslides are distributed relative to the background landscapes in upstream contributing area (A) space, with no assumptions of channel threshold A_{min} . To calculate ψ for each catchment, we integrated below the cumulative A distribution (cf. Figure 4a) to derive (i) an integrated area (IA_s) for the cumulative landslide volume- A distribution curve and (ii) an integrated area (IA_c) for the cumulative catchment DEM cell- A distribution curve. We then calculated each catchment’s landslide location index (ψ) as (Figures 4a and 4b):

$$\psi = \frac{IA_c}{IA_s} \quad (6)$$

For a higher ψ in a given catchment, the landslide inventory is preferentially located at larger upstream areas and should have a higher potential to connect to channels (Figures 4c and 4d). A medium ψ represents less potential for landslide-channel connection compared to a higher ψ regime (Figures 4e and 4f). A low ψ suggests low potential to connect to channels (Figures 4g and 4h). Since ψ considers where landslides are located with respect to the distribution of upstream contributing area in a catchment, higher values should reflect landslide positions characterized by greater flow accumulation for fixed hydrologic conditions.

4. Results and Discussion

4.1. Landscape Position and Connectivity of Wenchuan-Triggered Landslides

4.1.1. Cumulative Landslide Volume Curves

To gain a general perspective on the locations of landslides in relation to the morphology of the Longmen Shan catchments, we report the cumulative volumetric fraction of landslides as a function of upstream area

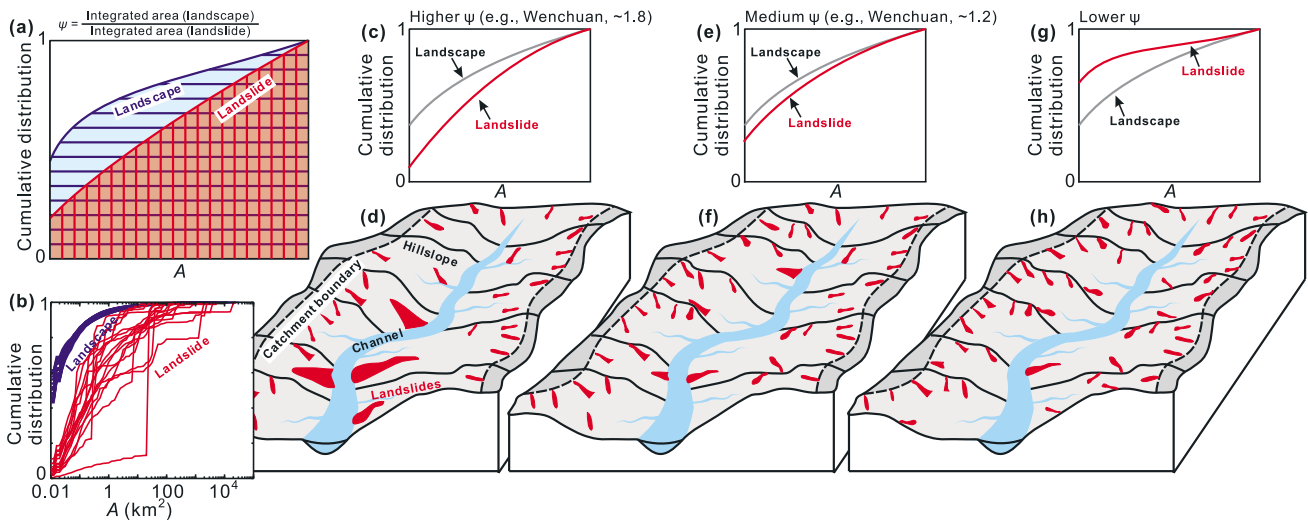


Figure 4. Illustration of catchment-scale landslide location index. (a) Schematic diagram illustrating landslide location index ψ , which is defined as the ratio of the integrated area below the catchment cumulative distribution curve as a function of upstream contributing area (blue) and the landslide volumetric distribution curve (red). (b) Compiled data from the study area; blue lines and red lines represent catchment and landslide distribution curves as a function of upstream area, respectively. (c) A case where most landslides occur at relatively high values of upstream contributing area A (e.g., $\psi \sim 1.8$ as seen in this study) compared to the landscape. (d) Cartoon illustration of Figure 4c. (e) A case where landslides are distributed fairly evenly across the catchment, similar to the catchment-scale distribution of A (e.g., $\psi \sim 1.2$ as seen in this study) compared to the landscape. (f) Cartoon illustration of Figure 4e. (g) A case where most landslides occur at relatively low values of upstream contributing area A compared to the landscape. (h) Cartoon illustration of Figure 4g. The Longmen Shan catchments affected by Wenchuan earthquake-triggered landslides are similar to Figures 4c and 4e.

(Figures 5 and S5). For all landslides in the study area, a high proportion of total landslide volume is located in the hillslope domain ($A < \sim 1 \text{ km}^2$, the threshold A_{min} for the Longmen Shan catchments), as indicated by the steep rise in cumulative volumetric fraction as a function of A for low values, i.e., $< 1 \text{ km}^2$ (Figure 5a). A lower proportion of total landslide volume (reflected by more gentle rise in the cumulative curves in Figure 5a) is located in the channel domain ($A > 1 \text{ km}^2$). For the three main catchments, different proportions of landslides in different domains lead to varied patterns in the cumulative volume curves. Large landslides introduce significant discontinuities to the distribution curves, because the nonlinear volume-area relationship ($\gamma > 1$) means that they contribute disproportionately to total sediment volume [Larsen *et al.*, 2010; Guzzetti *et al.*, 2009; Li *et al.*, 2014; Marc and Hovius, 2015]. The marked increase in landslide volume at $A \sim 30 \text{ km}^2$ (Figures 5a and 5d) is caused by the Daguangbao landslide, the largest landslide in the Wenchuan inventory, with an area of $\sim 7.2 \text{ km}^2$, around 2 orders of magnitudes larger than the median area [Chen *et al.*, 2014]. The Daguangbao landslide was located in the Kai Jiang tributary of the Fu Jiang catchment and causes discontinuities in the

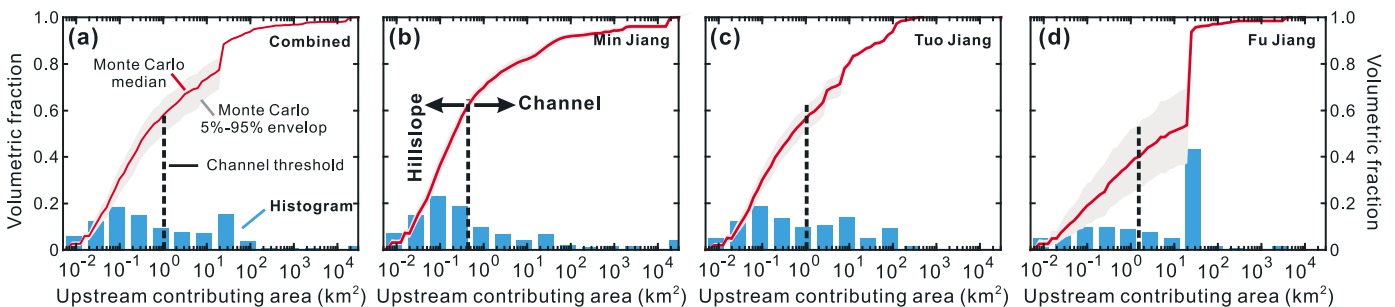


Figure 5. Cumulative distribution curves and histograms of landslide volumes over upstream contributing area. (a) Distribution curve and histogram for all landslides in the study area. (b) Distribution curve and histogram for landslides within the Min Jiang catchment. (c) Distribution curve and histogram for landslides within the Tuo Jiang catchment. (d) Distribution curve and histogram for landslides within the Fu Jiang catchment. The dashed black lines represent channel thresholds (determined from Figure 3); red curves represent the median results from 1000 Monte Carlo simulations propagating uncertainties in landslide area-volume scaling parameters; and grey bands are the 90% Monte Carlo envelope (5th–95th percentiles).

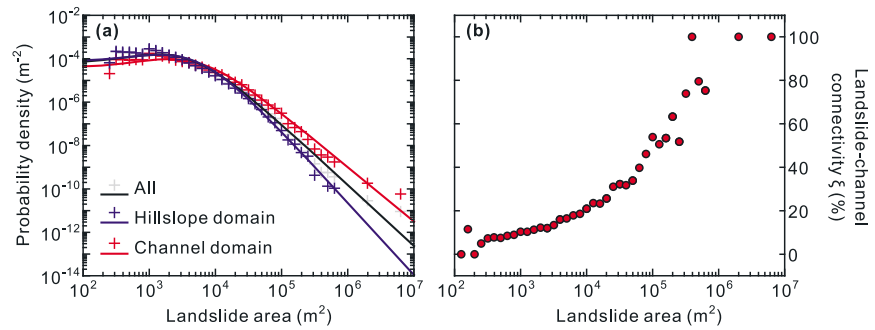


Figure 6. Statistical distribution of the Wenchuan coseismic landslides and landslide area control on landslide-channel connectivity. (a) Landslide probability density versus landslide area and the best fit three-parameter inverse-gamma functions for the landslide area probability density distributions. Grey symbols show the overall landslide inventory within the three main catchments, red symbols show the channel domain inventory, and blue symbols show the hillslope domain inventory. Black, red, and blue curves indicate best fit inverse-gamma functions to all landslides (best fit parameters: $q = 1.81$, $m = 7.62 \times 10^3 \text{ m}^2$, and $s = -1.31 \times 10^3 \text{ m}^2$, with $r^2 = 0.87$), channel-connected landslides (best fit parameters: $q = 1.51$, $m = 9.71 \times 10^3 \text{ m}^2$, and $s = -1.83 \times 10^3 \text{ m}^2$, with $r^2 = 0.84$), and hillslope-domain landslides (best fit parameters: $q = 2.32$, $m = 10.91 \times 10^3 \text{ m}^2$, and $s = -1.81 \times 10^3 \text{ m}^2$, with $r^2 = 0.83$), respectively. (b) Landslide size control on landslide-channel connectivity, showing a positive correlation between ζ and landslide area. Mean ζ values are calculated from landslide populations in each landslide area bin, with a bin size of $\delta \log_{10} A_{ls} = 0.1$.

distribution curves of these two catchments (Figure 5d and L10). For subcatchments and tributaries (L1–L17), two types of landslide distribution curves are observed (Figure S5): some catchments (e.g., L2 and L5) show similar patterns to the overall landslide inventory, while others (e.g., L7 and L16) are influenced by very large landslides with sharp rises in the V_s distribution curve in domains with higher upstream areas.

4.1.2. Region-Wide Connectivity Values

Based on the landslide upstream contributing area values and the threshold A_{min} values, we estimate that ~16% of the landslide population (in terms of number of landslides) is connected to river channels. Estimates of the number of channel-connected landslides associated with the Chi-Chi earthquake in Taiwan are lower (~8% of the total), while those triggered by Typhoon Herb are higher (~24%), a difference that may be attributed at least in part to clustering of coseismic landslides at hillslope crests [Dadson *et al.*, 2004]. As far as we are aware, directly comparable estimates of areal or volumetric connectivity are not available for the Chi-Chi earthquake or for other events.

For the Wenchuan-triggered landslides, 30% of total landslide area is connected to rivers, higher than the 16% population connectivity. The difference between these values indicates that larger landslides (by area) are more likely to be connected to channels. The Wenchuan landslide inventory follows a heavy-tailed distribution and can be fit by an inverse-gamma function (Figure 6) [e.g., Malamud *et al.*, 2004] defined by

$$p(A_{ls}; q, m, s) = \frac{1}{m\Gamma(q)} \left[\frac{m}{A_{ls} - s} \right]^{q+1} \exp \left[-\frac{m}{A_{ls} - s} \right] \quad (7)$$

where A_{ls} represents individual landslide areas, p is the probability density, and q , m , and s are inverse-gamma function parameters. Landslides in the hillslope and fluvial domains both follow inverse-gamma distributions (equation (7)), but with different parameters, indicating that landslides in the channel domain on average have larger areas than those in the hillslope domain (Figure 6a). Corroborating this interpretation, we group landslide populations based on areas and observe a well-defined positive correlation between average landslide area and average landslide-channel connectivity (Figure 6b). The influence of landslide area on connectivity is consistent with the expectation that, due to self-similar properties, larger landslides generally have longer lengths ($L \sim A_{ls}^{1/2}$) [Hovius *et al.*, 1997; Bellugi *et al.*, 2015] and are more likely to reach hillslope bases and connect to channels.

The volumetric connectivity of the Wenchuan-triggered landslides is $43 + 9/-7\%$ (median \pm 5th/95th percentiles from 1000 Monte Carlo simulations, propagating uncertainties from landslide area-volume scaling; Figure 5a). Volumetric connectivity is higher than areal connectivity because of the nonlinear area-volume scaling relationships and the above mentioned pattern of higher connectivity for larger area landslides. The remaining $57 + 7/-9\%$ of the total landslide volume is located, at least temporarily, on hillslopes.

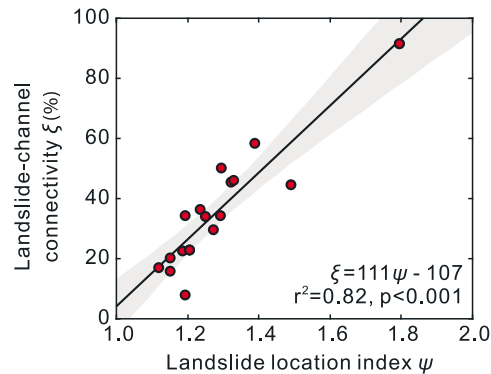


Figure 7. Relationship between landslide location index ψ and landslide-channel volumetric connectivity ζ . The solid line represents the best fit from linear regression, and the grey shading represent 95% confidence bands.

Because landslide-channel connectivity (ζ) and landslide location index (ψ) both quantify landslide distribution as functions of upstream area, ζ should theoretically correlate well with ψ . Connectivity (ζ) depends on the determination of channels, which might be complicated by multiple factors [Montgomery, 2001]. In contrast, location index (ψ) does not rely on how channels are defined and thus provides an independent representation of landslide location. For our data, the mean ζ in a given catchment is positively correlated with ψ ($r^2 = 0.82$, $p < 0.001$) (Figure 7), as we expect given that they represent similar characteristics of the landslide distribution. A principal difference between the two metrics is that, unlike ζ , the value of ψ will be influenced by the relative position of landslides with respect to distance from headwaters and thus to some extent with flow accumulation at the landslide locations. We may thus expect ψ to more generally reflect the influence of landslide position on sediment transport, a question we consider further in section 4.4.

4.3. What Determines the Connectivity of Wenchuan-Triggered Landslides?

4.3.1. Spatial Patterns of Landslide-Channel Connectivity

A central observation from our analysis is that landslide-channel connectivity is not uniform across the Wenchuan earthquake-affected region. In this section, we consider how and why connectivity varies spatially across the Longmen Shan. To illustrate the spatial patterns of the landslide inventory, we mapped areal densities for total landslides and channel-connected landslides, as well as landslide-channel connectivity over the three main study catchments (Figure 8). All landslides and channel-connected landslides have similar spatial distributions, with higher areal densities in the hanging wall of the Yingxiu-Beichuan fault and lower densities toward the Sichuan Basin and the plateau (Figures 8a and 8b) [e.g., Dai *et al.*, 2011; Gorum *et al.*, 2011]. The spatial pattern of landslide-channel connectivity is less distinct, although a clustering around the middle of the Yingxiu-Beichuan fault rupture is evident (Figure 8c).

When plotted in 5 km corridors along the steepest topographic gradient (A-A'), all landslides and channel-connected landslides show clear clustering around the Yingxiu-Beichuan fault (Figures 8d and 8e) [e.g., Dai *et al.*, 2011]. Except for some statistically less significant landslide groups (with landslide populations of < 20), landslide-channel connectivity shows a similar general trend, peaking around the Yingxiu-Beichuan fault and decaying toward the Sichuan Basin and the Tibetan Plateau (Figure 8f).

4.3.2. Controls on the Landslide-Channel Connectivity

The spatial variability in landslide-channel connectivity for the Wenchuan earthquake may provide general insight into what factors set the amount of landslide sediment delivered directly to river systems. To achieve high connectivity, landslides need to reach the hillslope base, and channel densities need to be high enough to sample a large number of landslides. Several factors may determine connectivity by influencing landslide sizes (and thus likelihood of reaching rivers) or regional channel densities. Here we focus on how topography, seismic intensity, and lithology influence landslide sizes, and on how topography and lithology influence channel densities. We explore each factor independently, acknowledging that there will be coupling and intercorrelation among them.

4.3.2.1. Topographic Control on Connectivity

To constrain the role of topography, we group landslides in the Wenchuan inventory by bins of mean gradient, mean elevation, and mean relief for all DEM cells within each landslide polygon extent, with bin sizes of 1° for gradient and 100 m for elevation and relief. We calculate the landslide-channel connectivity ζ within each group

4.2. Comparing Landslide Connectivity and Catchment-Scale Location Index

We calculated the catchment-scale landslide location index (ψ) for the 17 sub-catchments and tributaries impacted by landslides (Table 2). All ψ values, which range from 1.2 to 1.8, are greater than 1. The maximum ψ in the Wenchuan case is 1.8, for the Kai Jiang tributary, and is caused by the large Daguangbao landslide, which is located in the fluvial domain and contributes to the much lower IA_{15} (thus higher ψ) for this catchment.

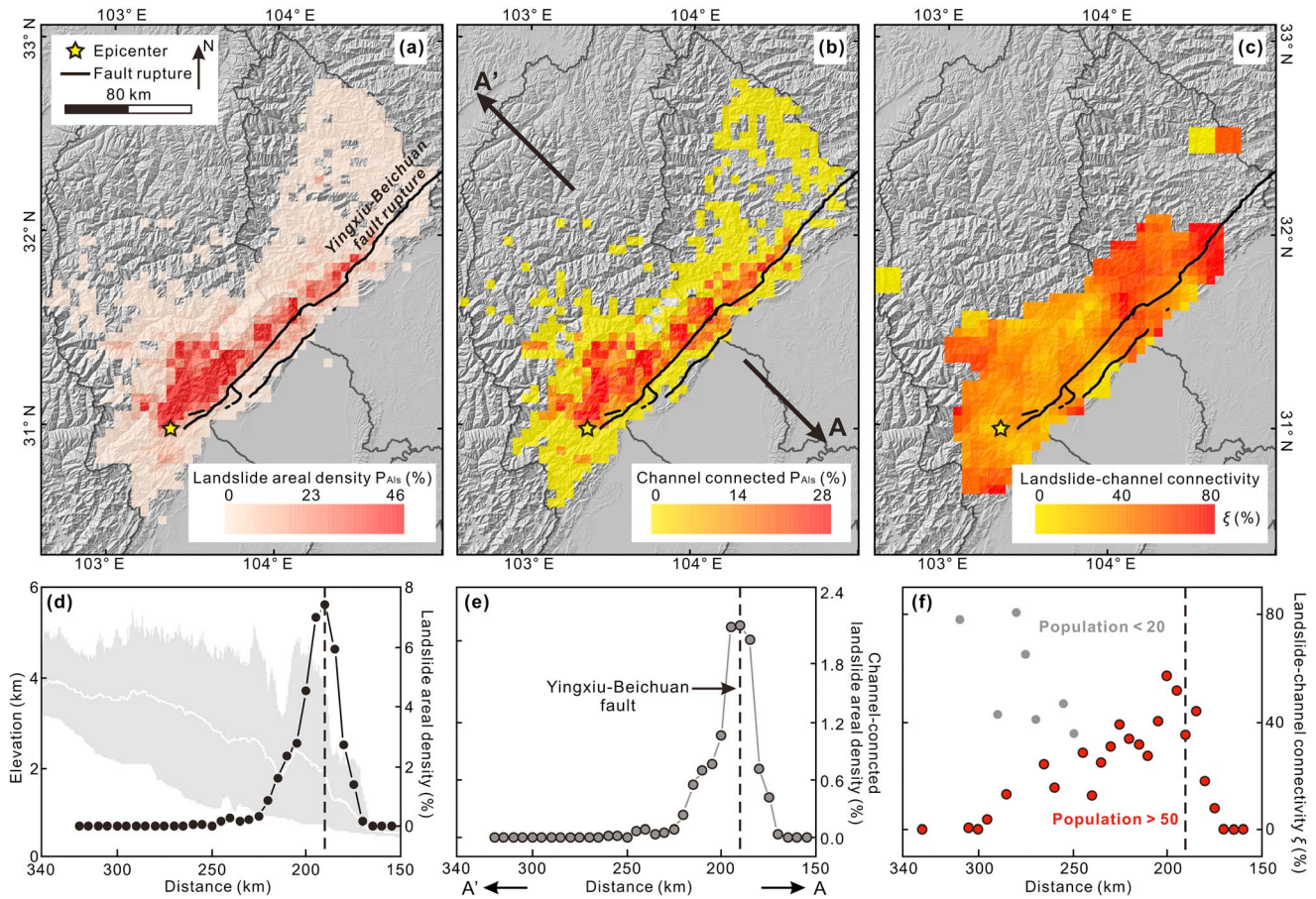


Figure 8. Spatial patterns of coseismic landslides, channel-connected landslides, and volumetric landslide-channel connectivity. (a) Distribution of coseismic landslide areal density P_{Als} in 5×5 km windows. The black lines show the extent of the Wenchuan surface rupture [Liu-Zeng *et al.*, 2009]. (b) Distribution of landslide areal density for channel-connected landslides in 5×5 km windows. A-A' indicates the swath trend defined in Figure 2. (c) Distribution of landslide-channel connectivity ζ (calculated from mean values of landslide area-volume scaling parameters) in 5×5 km windows. (d) Landslide areal density in 5 km corridors along swath A-A', superimposed on the swath profile of the Longmen Shan topography (mean, maximum, and minimum elevations). (e) Distribution of channel-connected landslide areal density in 5 km corridors along swath A-A'. (f) Landslide-channel connectivity ζ (calculated from mean values of landslide area-volume scaling parameters) in 5 km corridors along swath A-A'. Red dots represent landslide populations of numbers > 50 in each 5 km corridor, and grey dots show populations of < 20 . The black dashed line in Figures 8d–8f indicates the Yingxiu-Beichuan fault.

(Figures 9a–9c). Landslide-channel connectivity and landslide gradient (defined as the mean gradient for all DEM cells within each landslide polygon) show a well-defined negative trend (Figure 9a), except for a few landslides at the highest observed gradients. The general pattern of lower ζ as gradients increase can be attributed to the negative relationship between mean catchment gradient and drainage density (Figure S6a), implying a geomorphic control on channel distribution. High gradient areas have smaller upstream areas to support fluvial channels, thus leading to lower channel densities and lower landslide-channel connectivity. Gradients also have an effect on landslide size (Figure S6b) with steeper gradients facilitating larger landslides (meaning higher landslide-channel connectivity), competing with the gradient effect on drainage density. The overall negative trend between ζ and gradient indicates that the effect on drainage density is dominant. The effect of gradient on landslide size is most relevant for the steepest areas ($>60^\circ$) where a small fraction ($<1\%$) of landslides is located (grey dots in Figure S6b).

Elevation and relief couple tightly with gradient in the Longmen Shan. Low-elevation areas are limited to proximal valley floors and the Sichuan Basin, dominated by fluvial processes with dense fluvial networks (Figure 2g), leading to high probability for landslide-channel connection. Medium- to high-elevation areas represent mountain and plateau regions which have lower drainage density and are thus less prone to landslide-channel connection (Figures 2b and 9b). Similarly, lower relief occurs in either basin or plateau areas, with higher relief in between. Landslides in low-relief areas occur mostly in plateau regions where

drainage density and associated landslide-channel connectivity are low (Figure 9c). Medium-high relief areas are mainly found in the eastern Longmen Shan, where most earthquake-triggered landslides occurred, with medium-high drainage density, representing favorable conditions for landslide-channel connection (Figures 2g and 9c). Very high relief areas may represent some local areas with lower drainage density and consequently lower landslide-channel connectivity. Overall, the observed correlations suggest that topography influences landslide-channel connectivity mainly via controls on channel densities.

4.3.2.2. Lithological Control on Connectivity

We calculated ζ for different lithological units [China Geological Survey, 2004] grouped both (i) as metamorphic, igneous and sedimentary rocks, and (ii) as the main subtypes outcropping in the Longmen Shan range. The metamorphic rocks in the study area are mainly composed of low- to medium-grade units (e.g., slate, phyllite, schist, metasandstone, and marble). The major igneous rock is granitic. For sedimentary rocks, we identify three subtypes: carbonate, mudstone (fine clastic material), and sandstone (coarser clastic material). Across most lithologies, ζ is similar, but values are significantly higher for sandstone and mudstone and lower for slate (Figure 9d). In conjunction with other factors like precipitation, surface/subsurface hydrology, and topography, lithology influences drainage densities [Day, 1980; Tucker and Bras, 1998; Moglen et al., 1998; Duvall et al., 2004; Luo and Stepinski, 2008] and thus landslide-channel connectivity. We observe varied drainage density among different lithological units and a good correlation ($r^2 = 0.80$) between connectivity and drainage density of each lithological unit, excluding the < 2% landslide population from the slate unit (Figure 9e). Landslides in slate lithologies are mostly located at the northern end of the main fault rupture, in an area that is characterized by dominantly strike-slip fault motion, low topographic relief, and low peak ground acceleration (PGA), potentially explaining their anomalously low connectivity. Lithology-dependent rock strength might also influence landslide areas, and thus connectivity, but we did not find a statistically significant correlation between landslide area and connectivity among different lithologies. Our lithological classification is inevitably simplified and does not account for the complex interactions between lithology, rock strength, erodibility, and landsliding [Montgomery, 2001; Chen et al., 2011; Gallen et al., 2015]. Nonetheless, our observations point to a potential role for substrate properties in modulating landslide-landscape relations, particularly through setting drainage density.

4.3.2.3. Seismic Control on Connectivity

Previous studies have shown that the spatial distribution of earthquake-triggered landslides is determined by the patterns of peak ground acceleration (PGA) [e.g., Keefer, 1984; Jibson and Keefer, 1993; Meunier et al., 2007; Meunier et al., 2008; Kritikos et al., 2015]. Correlations between landslide densities and local PGA were also observed for the Wenchuan earthquake [Dai et al., 2011; Yuan et al., 2013; Gallen et al., 2015]. Here we find a positive correlation not only between landslide occurrence and PGA, as observed previously, but also between landslide-channel connectivity ζ and PGA (Figure 9f). This correlation can be explained by the observed dependence of individual landslide area on PGA (Figure S6c): higher seismic intensity and stronger ground motions tend to trigger larger landslides, which are more likely to reach channels. As expected, there is no correlation between PGA and drainage density (Figure S6d).

Spatial patterns of earthquake-triggered landslides are also sensitive to the sense of motion on the fault [Meunier et al., 2008; Barlow et al., 2015; Gorum and Carranza, 2015]. The Wenchuan landslides occurred in areas of complex faulting, varying along strike from dextral thrust to nearly pure strike-slip motion [Xu et al., 2009; Liu-Zeng et al., 2011; Gorum and Carranza, 2015]. We classified the Wenchuan landslides following the approach of Gorum and Carranza [2015], projecting landslides to the nearest segment of the fault rupture that was categorized based on the predominant type of motion (thrust, oblique slip, and strike slip) [Liu-Zeng et al., 2009]. We calculated the corresponding landslide-channel connectivity for the different types of faulting along each segment (Figure 9g). We acknowledge that landslides at any given site may be triggered by energy from different segments along the rupture, and not just by the nearest segment, but PGA values show limited variation along the main fault rupture, so we do not expect large biases.

The average landslide-channel connectivity for landslides in areas dominated by thrust and oblique-slip segments ($\zeta \sim 37 + 4/-3\%$, reported as median \pm 5th/95th percentiles from 1000 Monte Carlo simulations, propagating uncertainties from landslide area-volume scaling, and excluding the anomalously large Daguangbao landslide) is very slightly higher than for landslides adjacent to strike-slip segments ($\zeta \sim 32 \pm 1\%$) (Figure 9k). This finding is consistent with the fact that the mean landslide area near thrust and oblique-slip segments ($\sim 8300 \text{ m}^2$, excluding the Daguangbao landslide) is larger than that near strike-slip segments ($\sim 6300 \text{ m}^2$),

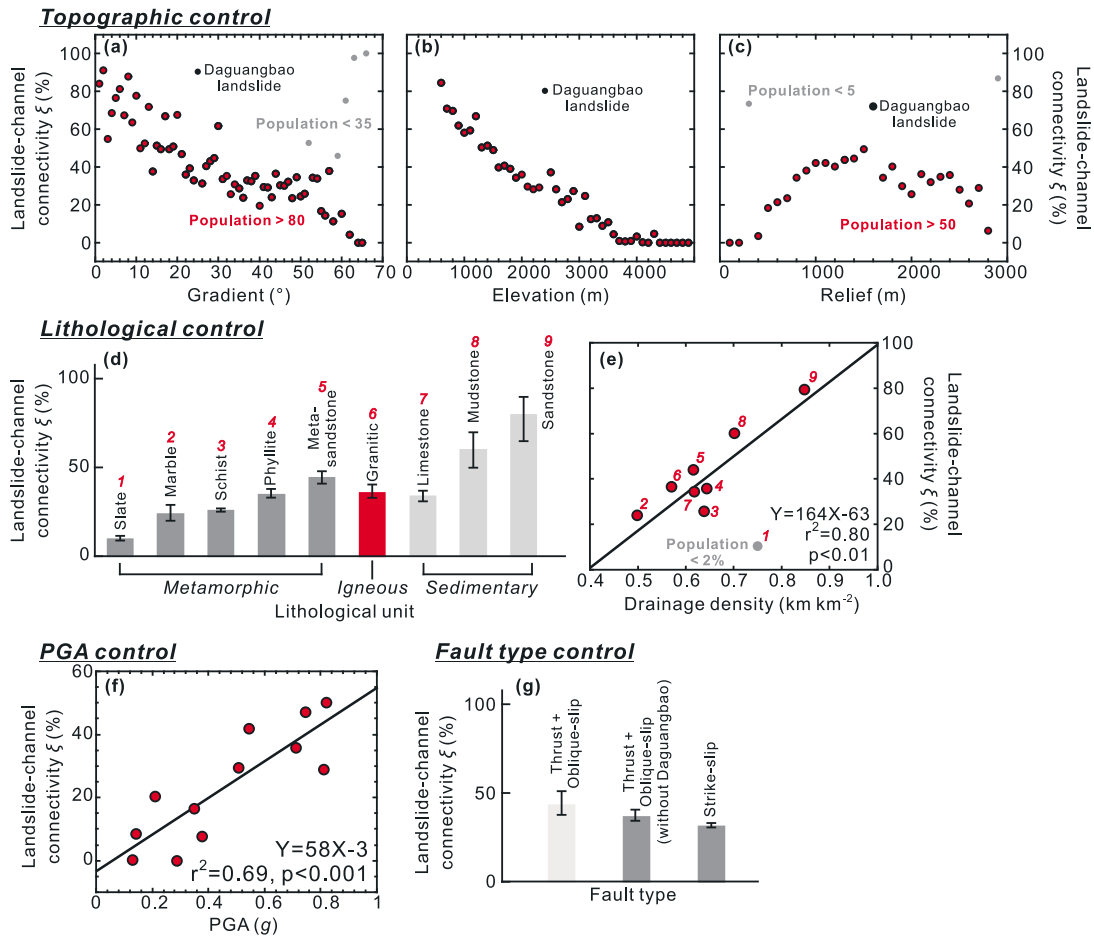


Figure 9. Controls on landslide-channel connectivity ξ . (a–c) Topographic control on landslide-channel connectivity. Mean ξ values are calculated from landslide populations in bins (δ) of each parameter, defined as follows: ξ versus gradient ($\delta = 1^{\circ}$) (Figure 9a), ξ versus elevation ($\delta = 100$ m) (Figure 9b), and ξ versus relief within a 2.5 km radius circular window ($\delta = 100$ m) (Figure 9c). Black dots indicate results from the very large Daguangbao landslide, while grey dots represent statistically less-represented groups (<1% of total landslide number). Note that the relief in Figure 9c may show local maximum relief not revealed in Figure 2d (averaged relief ± 1 standard deviation across the swath profile). (d) Lithological control on landslide-channel connectivity. Lithological data are taken from the 1: 2,500,000 China Geological Base Map [China Geological Survey, 2004]. Results are presented as median values (bars) and 90% envelopes (error bars, 5th–95th percentiles) from 1000 Monte Carlo simulations. (e) Dependence of landslide-channel connectivity on drainage density for landslides within each lithological unit. The grey dot represents <2% of the total landslide population. The black solid line represents the best linear fit, excluding the grey dot. Numbers aside each dot denote corresponding lithology as shown in Figure 9d. (f) Positive correlation between peak ground acceleration (PGA) and landslide-channel connectivity. The PGA and landslide-channel connectivity represent mean values calculated from 5 km wide increments along the swath profile A–A'. The solid line represents the best linear fit. (g) Fault-type control on landslide-channel connectivity. For landslides nearest to thrust and oblique-slip fault segments, the landslide-channel connectivity is reported for populations excluding the anomalously large Daguangbao landslide due to its significant, disproportional influence on the connectivity. Results are presented as median values (bars) and 90% envelopes (error bars, 5th–95th percentiles) from 1000 Monte Carlo simulations.

which may be explained by the spatial clustering of the seismic moment release around Yingxiu (dominated by thrust faulting) and Beichuan [Shen et al., 2009; Parker et al., 2011]. Several modeling studies have shown that, for the same magnitude of initial stress, thrust or reverse dip-slip faults can generate stronger ground motion compared to strike-slip faults [e.g., Oglesby and Day, 2002; Gabuchian et al., 2014]. Such relationships would mean both a higher susceptibility to landsliding and larger landslides, and consequently higher channel connectivity (Figure 6b), in thrust earthquakes compared to strike-slip events, consistent with the variations of landslide-channel connection that we observe.

4.3.2.4. Coupling of Effects

In some cases, the factors discussed above will be interrelated, for example, multiple factors could contribute to the observed lower connectivity for landslides in slate (Figure 9f), but their interrelations cannot be untangled with available data. Nonetheless, we do not observe highly systematic spatial correlations among

topography, lithology, and seismic parameters across the Longmen Shan, suggesting that our analysis still provides first-order insights into the roles of these parameters in controlling landslide-channel connectivity.

4.4. Implications for Post-Wenchuan Sediment Transport

For the Wenchuan case, 43 + 9/−7% of the coseismic landslide volume is directly connected to channels, representing ~1.4 km³ of the ~3 km³ total landslide volume in the Longmen Shan catchments. The remaining 57 + 7/−9% of landslide sediment volume (~1.6 km³) resides higher on hillslopes. This landslide-channel connectivity sets an initial condition for post-Wenchuan sediment transport. Channel-connected landslides are expected to have high potential for fluvial evacuation in the monsoonal climate [Liu-Zeng *et al.*, 2011; Wang *et al.*, 2015], whereas landslide material in the hillslope domain should be less immediately available for river transport [Meunier *et al.*, 2008; Dadson *et al.*, 2004; Hovius *et al.*, 2011; Huang and Fan, 2013; Tsai *et al.*, 2013]. These predictions can be tested by evaluating relationships between postearthquake sediment fluxes and the landslide inventory.

We currently lack constraints on bedload sediment transport following the Wenchuan earthquake, but Wang *et al.* [2015] reported suspended sediment (predominantly material <0.25 mm diameter) fluxes, allowing us to examine transport of the fine landslide material. We calculated the differences in suspended sediment fluxes for nested catchments reported in Wang *et al.* [2015], converting the total fluxes above each gauging station to a suspended sediment yield for individual subcatchments and tributary catchments (see details in supporting information). This approach returns negative values for 2 out of the 16 catchments where data are available, likely due to large sediment sinks such as reservoirs that are not accounted for in this analysis (catchments labeled as “N.A.” in Figure 10a and Table 3). These two catchments were excluded from the following analysis. For the other catchments, we normalized the estimated landslide density and sediment yield to the fraction of mountainous area (defined here as elevation > 800 m, Table 3) in the catchment. Several gauging stations located at further downstream sites also include large floodplain areas that contribute little to landsliding and sediment export, so we excluded these areas by using a threshold elevation.

Across the Longmen Shan catchments, we observe a positive correlation (Figure 10b, $r^2 = 0.40$, $p < 0.05$) between total landslide volumetric density P_{VLS} and postseismic (June 2008 to December 2008) suspended sediment yield. This relationship is consistent with landslides being a significant source of sediment following the earthquake. A similar positive correlation ($r^2 = 0.66$, $p < 0.05$) is observed between P_{VLS} and suspended sediment yield over the following 3 years (2009–2012) (Figure 10c). Although we do not account for postseismic landslides in our correlation analysis, we expect that the < ~20% additional postseismic landslide volume (see section 3.1 and Tang *et al.* [2011]) would not significantly affect our conclusions.

To examine the role of connectivity, we regressed P_{VLS} of channel-connected landslides with suspended sediment yield (Figures 10d and 10e). We find that there is no statistically significant difference in the correlation coefficients between total landslide density and suspended sediment yield on the one hand, and between channel-connected landslide density and suspended sediment yield on the other (examined by Meng's Z test ($p > 0.6$) [Meng *et al.*, 1992]). The correlation coefficients are statistically indistinguishable for total and channel-connected landslides whether considering the 2008 sediment flux data or the 2009–2012 data.

The normalized residuals from the regression between total landslide density and suspended sediment yield provide further insight into the possible role of connectivity in sediment transport. If landslide locations relative to channels play an important role in explaining postearthquake sediment fluxes, we should find that these residuals are positively related to connectivity or location index. Indeed, we find a weak but statistically significant relationship ($r^2 = 0.26$, $p < 0.1$) between residuals and location index (ψ) for the sediment yield measured in 2008 (Figure 10f). Connectivity (ζ) shows no similar correlation. By using a constant threshold area, the connectivity index does not account for the greater efficacy of sediment transport in higher-order channels, which is encapsulated in the location index, possibly explaining why ψ might better describe the potential for sediment transport. Nonetheless, the relationship between the residuals and ψ disappears for the sediment yield measured between 2009 and 2012 (Figure 10g). We speculate that this observation can be explained by an initially weak influence of landslide location on fine sediment fluxes (as observed in the 2008 data), with the influence of landslide locations fading over time. This could be because fine-grained landslide material is relatively readily entrained from landslide deposits even in the hillslope domain, for example, via overland flow during monsoonal storms over the 2009–2012 time period, such that landslide locations become less relevant. It is also possible that

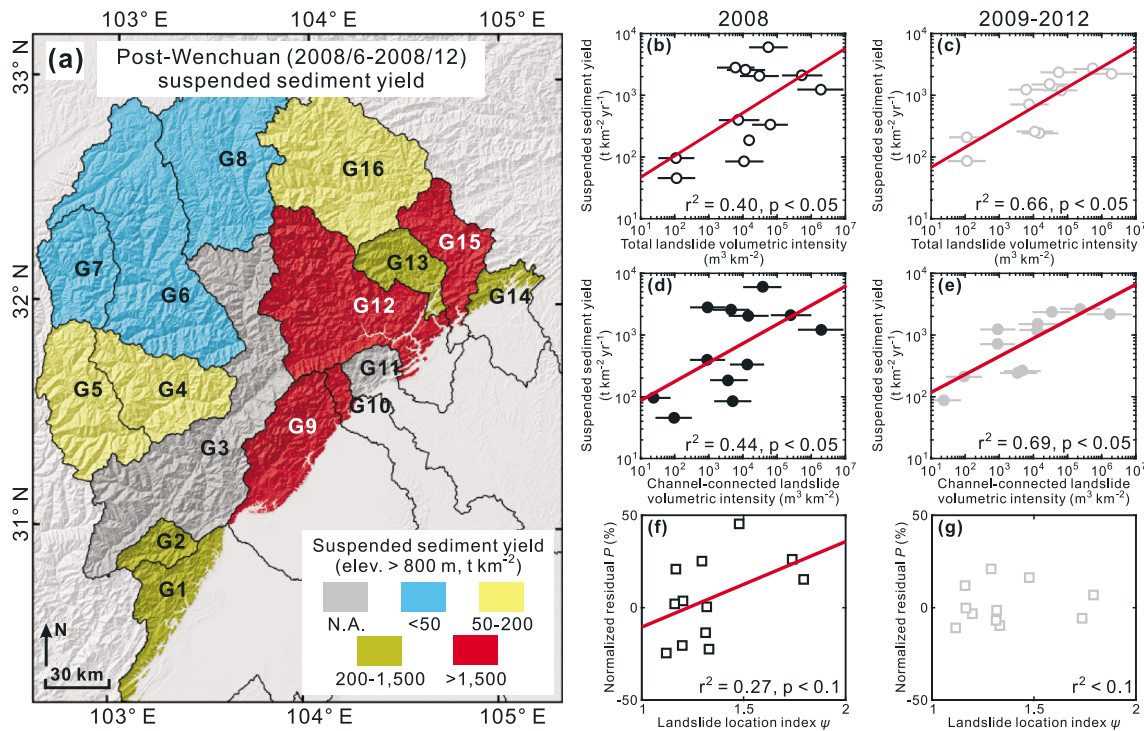


Figure 10. Spatial pattern of post-Wenchuan suspended sediment yield and relations to coseismic landslide volumetric density (equation (4)). (a) Distribution of postearthquake suspended sediment yield (t km^{-2}) in catchments across the Longmen Shan range (integrated over June 2008 to December 2008, based on data from Wang *et al.* [2015]), normalized for areas with elevation > 800 m, with color coding of the derived suspended sediment yield. Catchments labeled N.A. indicate negative-valued calculated sediment yield due to unaccounted large sediment sinks like reservoirs (see supporting information). (b and d) Sediment yield over June 2008 to December 2008 (normalized to 1 year) plotted versus total landslide volumetric density (Figure 10b) and channel-connected landslide volumetric density (Figure 10d) for each catchment; solid lines show power law best fit as determined from least squares fit in the logarithm space. (c and e) Annual sediment yield over 2009–2012 plotted against total landslide volumetric density (Figure 10c) and channel-connected landslide volumetric density (Figure 10e) for each catchment; solid lines show power law best fit as determined from least squares fit in logarithmic space. (f and g) Relations of normalized residual (P) from the fit between total landslide density and sediment yield versus the corresponding landslide location index (ψ) using the 2008 data (Figure 10f) and 2009–2012 data (Figure 10g), respectively. The solid line in Figure 10f shows the best fit between the normalized residual and location index using the 2008 data.

any signal in the 2009–2012 data is convoluted by other effects, including postseismic landslides, although we expect these to make a relatively minor contribution as discussed above.

Fine sediment only represents a small proportion (< 10 wt %) of the total volume of material from Wenchuan earthquake-triggered landslides, leaving coarse material (> 0.25 mm) as the dominant component [Wang *et al.*, 2015]. We expect that the supply of coarse material to river channels may be more affected by landslide-channel connectivity than the supply of fine-grained material, since coarse material is likely to be less easily mobilized from hillslopes. We currently do not have data constraining coarse sediment fluxes from multiple catchments in the Longmen Shan, but such information would be valuable for more completely testing conceptual models for landslide sediment transport.

5. Conclusions

We have systematically explored the locations of landslides triggered by the 2008 Wenchuan earthquake within the fluvial network across the Longmen Shan range at the eastern edge of the Tibetan Plateau. We quantified landslide-channel connectivity in terms of landslide volume, area, and number, and we examined how volumetric connectivity ζ varies spatially in order to understand what controls the supply of sediment for fluvial evacuation. Finally, we have considered our connectivity results in the context of sediment transport following the Wenchuan earthquake. Several key findings contribute to better understanding of coseismic landslides as sediment sources:

1. For the coseismic landslide inventory within the three main catchments draining the Longmen Shan (covering over 90% of the total landslide-impacted area), 16% of the total landslide number, 30% of the

Table 3. Compiled Data for Postearthquake Suspended Sediment Yields and Landslide Volumetric Densities

Large Catchment	ID	Catchment Notation	Catchment Type	Fraction of Mountainous Area (Elevation > 800 m) in Total Catchment Area	Controlling Hydrological Station ^a
Min Jiang	G1	Min Jiang Pengshan to Dujiangyan	Subcatchment	0.19	Pengshan
	G2	Guojiaba	Tributary	1	Guojiaba
	G3	Min Jiang Dujiangyan to Zhenjiangguan	Subcatchment	1	Dujiang
	G4	Lower Zagunao	Tributary	1	Sangping
	G5	Upper Zagunao	Tributary	1	Zagunao
	G6	Lower Heishui	Tributary	1	Shaba
	G7	Upper Heishui	Tributary	1	Heishui
	G8	Min Jiang above Zhenjiangguan	Subcatchment	1	Zhenjiangguan
Tuo Jiang	G9	Tuo Jiang main	Main catchment	0.14	Dengyingyan
Fu Jiang	G10	Kai Jiang above Santai	Tributary	0.10	Santai
	G11	Fu Jiang Shehong to Fujiangqiao	Subcatchment	0.16	Shehong
	G12	Fu Jiang Fujiangqiao to Jiangyou	Subcatchment	0.85	Fujiangqiao
	G13	Pingtong He above Ganxi	Tributary	0.98	Ganxi
	G14	Upper Zitong Jiang above Zitong	Tributary	0.26	Zitong
	G15	Fu Jiang Jiangyou to Pingwu	Subcatchment	0.93	Jiangyou
	G16	Fu Jiang above Pingwu	Subcatchment	1	Pingwu

^aDetailed information on hydrological stations is reported in Wang *et al.* [2015].

^bPost-Wenchuan (June 2008 to December 2008) suspended sediment yield is the total suspended sediment yield from June 2008 to December 2008 based on the data set from the hydrological stations [Wang *et al.*, 2015]; 1σ uncertainty is propagated from uncertainties in the original hydrological data set.

^cPost-Wenchuan (2009–2012) annual suspended sediment yield is the annual mean sediment yield during 2009–2012 based on the data set from the hydrological stations [Wang *et al.*, 2015]; 1σ uncertainty is propagated from uncertainties in original hydrological data set.

^dTotal landslide density is calculated as landslide volume/catchment area (equation (4)); Monte Carlo simulations are run for propagating uncertainties from parameters in landslide area-volume scaling and reported as the medians and the 16th and the 84th percentiles [Li *et al.*, 2014].

^eChannel-connected landslide volumetric density is calculated as channel-connected landslide volume/catchment area (equation (4)); Monte Carlo simulations are run for propagating uncertainties from parameters in landslide area-volume scaling and reported as the medians and the 16th and the 84th percentiles [Li *et al.*, 2014].

^fSediment yield is not available because the calculations return negative values; see main text.

^gLandslide data are not available due to no coverage of satellite imagery.

^hLandslide location index is not available due to no landslide data.

total landslide area, and 43 + 9/–7% of the total landslide volume (~1.4 km³) are directly connected to fluvial channels and thus prone to entrainment and transport by rivers. The remaining 57 + 7/–9% by volume (~1.6 km³) was deposited higher on hillslopes, beyond the immediate extent of the fluvial channel network. If connectivity plays an important role in sediment dynamics, we would expect this material to be unavailable for immediate transport.

2. The catchment landslide location index ψ , which describes the relative distribution of landslides versus catchment topography as a function of upstream contributing area, provides an additional constraint on landslide locations in landscapes independent of channel definition. We find a positive correlation across different catchments between ψ and our determination of landslide-channel connectivity (ζ) based on gradient-upstream area relations, suggesting these metrics are consistent. We suggest that ψ may provide a complementary index that also reflects upstream area and thus may capture the more general influence of landslide position on sediment transport, as hinted by sediment flux data following the Wenchuan earthquake.
3. Landslide-channel connectivity is linked to topographic parameters, specifically to gradient and drainage density, which are themselves correlated. Lithology is also an important control on connectivity, with higher volumetric landslide-channel connectivity ($\zeta \sim 60\text{--}80\%$) for clastic sedimentary bedrock and lower (10–20%) for high-grade metamorphic bedrock. Our analysis also suggests higher landslide-channel connectivity in areas with higher PGA and near fault segments dominated by thrust and oblique slip during the Wenchuan earthquake. The coupling of these factors may also contribute to the observed landslide-channel connectivity pattern.
4. The correlation between suspended sediment yield and the volumetric density of channel-connected landslides is statistically indistinguishable from the correlation with the volumetric density of all landslides. Residuals from the correlation between sediment yield and the density all landslides are weakly related to location index ψ for data from 2008, immediately following the earthquake, but not to location index for data from the ensuing years. This suggests a weak initial influence of connectivity on fine-

Table 3. (continued)

Post-Wenchuan (June 2008 to December 2008) Suspended Sediment Yield ^b (t km ⁻²)	Post-Wenchuan (2009–2012) Annual Suspended Sediment Yield ^c (t km ⁻² yr ⁻¹)	Total Landslide Volumetric Density ^d (×10 ³ m ³ km ⁻²)	Channel-Connected Landslide Volumetric Density ^e (×10 ³ m ³ km ⁻²)	Landslide Location Index ψ
1194 ± 133	1494 ± 389	27.83 + 70.87/–19.55	12.46 + 36.51/–9.08	1.31
195 ± 19	1202 ± 120	61.74 + 127.16/–42.10	12.23 + 25.50/–8.43	1.17
N.A. ^f	N.A. ^f	251.37 + 585.53/–180.94	76.20 + 182.57/–55.47	1.28
108 ± 17	242 ± 59	14.80 + 37.90/–10.31	3.44 + 9.15/–2.42	1.29
50 ± 5	259 ± 26	10.61 + 25.88/–7.43	4.59 + 11.46/–3.25	1.48
56 ± 7	87 ± 17	0.11 + 0.24/–0.07	0.02 + 0.05/–0.01	1.17
27 ± 3	210 ± 21	0.11 + 0.25/–0.08	0.09 + 0.21/–0.06	1.74
19 ± 2	173 ± 17	N.A. ^g	N.A. ^g	N.A. ^h
1227 ± 123	2658 ± 266	500.72 + 1371.63/–359.46	214.87 + 637.43/–158.08	1.32
715 ± 71	2164 ± 216	1826.49 + 6103.69/–1422.71	1655.16 + 5774.35/–1303.56	1.79
N.A. ^f	N.A. ^f	376.03 + 942.51/–264.55	128.77 + 336.19/–92.08	1.26
3496 ± 475	2343 ± 318	54.74 + 132.72/–38.84	33.85 + 85.70/–24.56	1.33
1641 ± 164	1226 ± 123	5.96 + 13.97/–4.14	0.87 + 2.02/–0.60	1.12
3210 ± 321	1537 ± 154	N.A. ^g	N.A. ^g	N.A. ^h
1504 ± 226	N.A. ^f	12.03 + 28.81/–8.46	4.13 + 9.86/–2.91	1.19
231 ± 23	708 ± 71	7.34 + 20.39/–5.26	0.86 + 1.93/–0.59	1.20

sediment fluxes that decreases over time. This observation may be related to mobilization of fine-grained material from hillslopes, and future work needs to establish whether the fluvial transport of coarser fractions of landslide debris is affected more significantly by landslide locations.

Overall, our results shed light on landslide locations in landscapes and how landslide-channel connection regulates sediment transport after large earthquakes. This work provides an important database for future research on sediment dynamics following the Wenchuan earthquake. The framework and methodology developed in this study are also applicable to other earthquakes in similar settings, promising greater understanding of the role of rare, high-magnitude seismic events in regulating sediment transport processes, in influencing associated sediment-related hazards, and in the long-term tectonic and topographic evolution of mountain belts.

Acknowledgments

This research was supported by the U.S. National Science Foundation (NSF-EAR/GLD grant 1053504 to A.J.W.) and the Chinese Academy of Sciences (YIS fellowship grant 2011Y2ZA04 to A.J.W.). G. L. was supported by a USC college merit fellowship and a GSA graduate research grant. We thank the NSF-supported Polar Geospatial Center for providing DigitalGlobe imagery. The landslide inventory data are available upon request. Constructive comments from the Associate Editor, Isaac Larsen, and two anonymous reviewers greatly helped to improve an earlier version of the manuscript. This work also benefited from conversations with Niels Hovius, Dimitri Lague, Patrick Meunier, Marc Odin, and Joel Scheingross.

References

- Allen, R. B., P. J. Bellingham, and S. K. Wiser (1999), Immediate damage by an earthquake to a temperate montane forest, *Ecology*, *80*(2), 708–714, doi:10.1890/0012-9658(1999)080[0708:idbaet]2.0.co;2.
- Attal, M., and J. Lavé (2006), Changes of bedload characteristics along the Marsyandi River (central Nepal): Implications for understanding hillslope sediment supply, sediment load evolution along fluvial networks, and denudation in active orogenic belts, *Geol. Soc. Am. Spec. Pap.*, *398*, 143–171, doi:10.1130/2006.2398(09).
- Barlow, J., I. Barisin, N. Rosser, D. Petley, A. Densmore, and T. Wright (2015), Seismically-induced mass movements and volumetric fluxes resulting from the 2010 M_w 7.2 earthquake in the Sierra Cucapah, Mexico, *Geomorphology*, *230*, 138–145, doi:10.1016/j.geomorph.2014.11.012.
- Bellugi, D., D. G. Milledge, W. E. Dietrich, J. A. McKean, J. T. Perron, E. B. Sudderth, and B. Kazian (2015), A spectral clustering search algorithm for predicting shallow landslide size and location, *J. Geophys. Res. Earth Surf.*, *120*, 300–324, doi:10.1002/2014JF003137.
- Brardinoni, F., and M. A. Hassan (2006), Glacial erosion, evolution of river long profiles, and the organization of process domains in mountain drainage basins of coastal British Columbia, *J. Geophys. Res.*, *111*, F01013, doi:10.1029/2005JF003358.
- Burchfiel, B. C., C. Zhiliang, L. Yupinc, and L. H. Royden (1995), Tectonics of the Longmen Shan and adjacent regions, Central China, *Int. Geol. Rev.*, *37*(8), 661–735, doi:10.1080/00206819509465424.
- Burchfiel, B. C., L. H. Royden, R. D. van der Hilst, B. H. Hager, Z. Chen, R. W. King, C. Li, J. Lü, H. Yao, and E. Kirby (2008), A geological and geophysical context for the Wenchuan earthquake of 12 May 2008, Sichuan, People's Republic of China, *GSA Today*, *18*(7), 5, doi:10.1130/GSATG18A.1.
- Chen, H., G.-W. Lin, M.-H. Lu, T.-Y. Shih, M.-J. Horng, S.-J. Wu, and B. Chuang (2011), Effects of topography, lithology, rainfall and earthquake on landslide and sediment discharge in mountain catchments of southeastern Taiwan, *Geomorphology*, *133*(3–4), 132–142, doi:10.1016/j.geomorph.2010.12.031.
- Chen, Q., H. Cheng, Y. Yang, G. Liu, and L. Liu (2014), Quantification of mass wasting volume associated with the giant landslide Daguangbao induced by the 2008 Wenchuan earthquake from persistent scatter InSAR, *Remote Sens. Environ.*, *152*, 125–135, doi:10.1016/j.rse.2014.06.002.
- China Geological Survey (2004), *China Geological Base Map and Instructions (1:2,500,000)*, edited by K. Huang, SinoMaps Press, Beijing.
- Clark, K. E., et al. (2016), Storm-triggered landslides in the Peruvian Andes and implications for topography, carbon cycles, and biodiversity, *Earth Surf. Dyn.*, *4*(1), 47–70, doi:10.5194/esurf-4-47-2016.
- Crudden, D. M., and D. J. Varnes (1996), Landslide types and processes, in *Landslides: Investigation and Mitigation, Transportation Research Board*, vol. 247, edited by Turner, A. K., and Schuster, R. L., Chap. 3, pp. 36–75, Natl. Res. Council, Natl. Acad. Press, Washington, D. C.

- Cui, Y., G. Parker, J. Pizzuto, and T. E. Lisle (2003), Sediment pulses in mountain rivers: 2. Comparison between experiments and numerical predictions, *Water Resour. Res.*, 39(9), 1240, doi:10.1029/2002WR001805.
- Dadson, S. J., et al. (2004), Earthquake-triggered increase in sediment delivery from an active mountain belt, *Geology*, 32(8), 733–736, doi:10.1130/G20639.1.
- Dai, F. C., C. Xu, X. Yao, L. Xu, X. B. Tu, and Q. M. Gong (2011), Spatial distribution of landslides triggered by the 2008 M_s 8.0 Wenchuan earthquake, China, *J. Asian Earth Sci.*, 40(4), 883–895, doi:10.1016/j.jseae.2010.04.010.
- Day, D. G. (1980), Lithologic controls of drainage density, *CATENA*, 7(1), 339–351, doi:10.1016/S0341-8162(80)80024-5.
- Densmore, A. L., and N. Hovius (2000), Topographic fingerprints of bedrock landslides, *Geology*, 28(4), 371–374, doi:10.1130/0091-7613(2000)28<371:tfobl>2.0.co;2.
- Densmore, A. L., M. A. Ellis, Y. Li, R. J. Zhou, G. S. Hancock, and N. Richardson (2007a), Active tectonics of the Beichuan and Pengguan faults at the eastern margin of the Tibetan Plateau, *Tectonics*, 26, TC4005, doi:10.1029/2006TC001987.
- Densmore, A. L., S. Gupta, P. A. Allen, and N. H. Dawers (2007b), Transient landscapes at fault tips, *J. Geophys. Res.*, 112, F03508, doi:10.1029/2006JF000560.
- DiBiase, R. A., K. X. Whipple, A. M. Heimsath, and W. B. Ouimet (2010), Landscape form and millennial erosion rates in the San Gabriel Mountains, CA, *Earth Planet. Sci. Lett.*, 289(1–2), 134–144, doi:10.1016/j.epsl.2009.10.036.
- Dingman, S. L. (1978), Drainage density and streamflow: A closer look, *Water Resour. Res.*, 14(6), 1183–1187, doi:10.1029/WR014i006p01183.
- Duvall, A., E. Kirby, and D. Burbank (2004), Tectonic and lithologic controls on bedrock channel profiles and processes in coastal California, *J. Geophys. Res.*, 109, F03002, doi:10.1029/2003JF000086.
- Egholm, D. L., M. F. Knudsen, and M. Sandiford (2013), Lifespan of mountain ranges scaled by feedbacks between landsliding and erosion by rivers, *Nature*, 498(7455), 475–478, doi:10.1038/Nature12218.
- Ferguson, R. I., M. Church, C. D. Rennie, and J. G. Venditti (2015), Reconstructing a sediment pulse: Modeling the effect of placer mining on Fraser River, Canada, *J. Geophys. Res. Earth Surf.*, 120, 1436–1454, doi:10.1002/2015JF003491.
- Fielding, E. J., A. Sladen, Z. H. Li, J. P. Avouac, R. Burgmann, and I. Ryder (2013), Kinematic fault slip evolution source models of the 2008 $M7.9$ Wenchuan earthquake in China from SAR interferometry, GPS and teleseismic analysis and implications for Longmen Shan tectonics, *Geophys. J. Int.*, 194(2), 1138–1166, doi:10.1093/Gji/Ggt155.
- Gabuchian, V., A. J. Rosakis, N. Lapusta, and D. D. Oglesby (2014), Experimental investigation of strong ground motion due to thrust fault earthquakes, *J. Geophys. Res. Solid Earth*, 119, 1316–1336, doi:10.1002/2013JB010409.
- Gallen, S. F., M. K. Clark, and J. W. Godt (2015), Coseismic landslides reveal near-surface rock strength in a high-relief, tectonically active setting, *Geology*, 43(1), 11–14, doi:10.1130/g36080.1.
- Garwood, N. C., D. P. Janos, and N. Brokaw (1979), Earthquake-caused landslides: A major disturbance to tropical forests, *Science*, 205(4410), 997–999, doi:10.1126/science.205.4410.997.
- Glade, T., and M. J. Crozier (2005), The nature of landslide hazard impact, in *Landslide Hazard and Risk*, pp. 41–74, John Wiley, Chichester.
- Godard, V., J. Lave, J. Carcaillet, R. Cattin, D. Bourles, and J. Zhu (2010), Spatial distribution of denudation in Eastern Tibet and regressive erosion of plateau margins, *Tectonophysics*, 491(1–4), 253–274, doi:10.1016/j.tecto.2009.10.026.
- Gorum, T., and E. J. M. Carranza (2015), Control of style-of-faulting on spatial pattern of earthquake-triggered landslides, *Int. J. Environ. Sci. Technol.*, 1–24, doi:10.1007/s13762-015-0752-y.
- Gorum, T., X. M. Fan, C. J. van Westen, R. Q. Huang, Q. Xu, C. Tang, and G. H. Wang (2011), Distribution pattern of earthquake-induced landslides triggered by the 12 May 2008 Wenchuan earthquake, *Geomorphology*, 133(3–4), 152–167, doi:10.1016/j.geomorph.2010.12.030.
- Guzzetti, F., F. Ardizzone, M. Cardinali, M. Rossi, and D. Valigi (2009), Landslide volumes and landslide mobilization rates in Umbria, central Italy, *Earth Planet. Sci. Lett.*, 279(3–4), 222–229, doi:10.1016/j.epsl.2009.01.005.
- Hilton, R. G., P. Meunier, N. Hovius, P. J. Bellingham, and A. Galy (2011), Landslide impact on organic carbon cycling in a temperate montane forest, *Earth Surf. Processes Landforms*, 36(12), 1670–1679, doi:10.1002/Esp.2191.
- Hovius, N., C. P. Stark, and P. A. Allen (1997), Sediment flux from a mountain belt derived by landslide mapping, *Geology*, 25(3), 231–234, doi:10.1130/0091-7613(1997)025<0231:sffamb>2.3.co;2.
- Hovius, N., P. Meunier, L. Ching-Weei, C. Hongey, C. Yue-Gau, S. Dadson, H. Ming-Jame, and M. Lines (2011), Prolonged seismically induced erosion and the mass balance of a large earthquake, *Earth Planet. Sci. Lett.*, 304(3–4), 347–355, doi:10.1016/j.epsl.2011.02.005.
- Huang, A. Y. L., and D. R. Montgomery (2014), Topographic locations and size of earthquake- and typhoon-generated landslides, Tachia River, Taiwan, *Earth Surf. Processes Landforms*, 39(3), 414–418, doi:10.1002/esp.3510.
- Huang, R. Q., and X. M. Fan (2013), The landslide story, *Nat. Geosci.*, 6(5), 325–326, doi:10.1038/ngeo1806.
- Jarvis, A., H. I. Reuter, A. Nelson, and E. Guevara (2008), Hole-filled SRTM for the globe version 4. [Available at the CGIAR-CSI SRTM 90 m Database (<http://srtm.csi.cgiar.org>)]
- Jibson, R. W., and D. K. Keefer (1993), Analysis of the seismic origin of landslides: Examples from the New Madrid seismic zone, *Geol. Soc. Am. Bull.*, 105(4), 521–536, doi:10.1130/0016-7606(1993)105<0521:aotsoo>2.3.co;2.
- Jin, Z., A. J. West, F. Zhang, Z. An, R. G. Hilton, J. Yu, J. Wang, G. Li, L. Deng, and X. Wang (2016), Seismically enhanced solute fluxes in the Yangtze River headwaters following the A.D. 2008 Wenchuan earthquake, *Geology*, 44(1), 47–50, doi:10.1130/g37246.1.
- Keefer, D. K. (1984), Landslides caused by earthquakes, *Geol. Soc. Am. Bull.*, 95(4), 406–421, doi:10.1130/0016-7606(1984)95<406:LCBE>2.0.CO;2.
- Keefer, D. K. (1994), The importance of earthquake-induced landslides to long-term slope erosion and slope-failure hazards in seismically active regions, *Geomorphology*, 10(1–4), 265–284, doi:10.1016/0169-555x(94)90021-3.
- Kirby, E., K. X. Whipple, W. Tang, and Z. Chen (2003), Distribution of active rock uplift along the eastern margin of the Tibetan Plateau: Inferences from bedrock channel longitudinal profiles, *J. Geophys. Res.*, 108(B4), 2217, doi:10.1029/2001JB000861.
- Kirby, E., K. Whipple, and N. Harkins (2008), Topography reveals seismic hazard, *Nat. Geosci.*, 1(8), 485–487.
- Korup, O., M. J. McSaveney, and T. R. H. Davies (2004), Sediment generation and delivery from large historic landslides in the Southern Alps, New Zealand, *Geomorphology*, 61(1–2), 189–207, doi:10.1016/j.geomorph.2004.01.001.
- Korup, O., J. J. Clague, R. L. Hermanns, K. Hewitt, A. L. Strom, and J. T. Weidinger (2007), Giant landslides, topography, and erosion, *Earth Planet. Sci. Lett.*, 261(3–4), 578–589, doi:10.1016/j.epsl.2007.07.025.
- Kritikos, T., T. R. Robinson, and T. R. H. Davies (2015), Regional coseismic landslide hazard assessment without historical landslide inventories: A new approach, *J. Geophys. Res. Earth Surf.*, 120, 711–729, doi:10.1002/2014JF003224.
- Larsen, I. J., D. R. Montgomery, and O. Korup (2010), Landslide erosion controlled by hillslope material, *Nat. Geosci.*, 3(4), 247–251, doi:10.1038/ngeo776.
- Larsen, I. J., D. R. Montgomery, and H. M. Greenberg (2014), The contribution of mountains to global denudation, *Geology*, 42(6), 527–530, doi:10.1130/g35136.1.

- Li, G., A. J. West, A. L. Densmore, Z. Jin, R. N. Parker, and R. G. Hilton (2014), Seismic mountain building: Landslides associated with the 2008 Wenchuan earthquake in the context of a generalized model for earthquake volume balance, *Geochem. Geophys. Geosyst.*, *15*, 833–844, doi:10.1002/2013GC005067.
- Li, Y., P. A. Allen, A. L. Densmore, and X. Qiang (2003), Evolution of the Longmen Shan Foreland Basin (Western Sichuan, China) during the Late Triassic Indosinian Orogeny, *Basin Res.*, *15*(1), 117–138, doi:10.1046/j.1365-2117.2003.00197.x.
- Liu, F., J. Li, and S. Yang (2015), Landslide erosion associated with the Wenchuan earthquake in the Minjiang River watershed: Implication for landscape evolution of the Longmen Shan, eastern Tibetan Plateau, *Nat. Hazards*, *76*(3), 1911–1926, doi:10.1007/s11069-014-1575-8.
- Liu-Zeng, J., et al. (2009), Co-seismic ruptures of the 12 May 2008, M_s 8.0 Wenchuan earthquake, Sichuan: East-west crustal shortening on oblique, parallel thrusts along the eastern edge of Tibet, *Earth Planet. Sci. Lett.*, *286*(3–4), 355–370, doi:10.1016/j.epsl.2009.07.017.
- Liu-Zeng, J., L. Wen, M. Oskin, and L. S. Zeng (2011), Focused modern denudation of the Longmen Shan margin, eastern Tibetan Plateau, *Geochem. Geophys. Geosyst.*, *12*, Q11007, doi:10.1029/2011GC003652.
- Luo, W., and T. Stepinski (2008), Identification of geologic contrasts from landscape dissection pattern: An application to the Cascade Range, Oregon, USA, *Geomorphology*, *99*(1–4), 90–98, doi:10.1016/j.geomorph.2007.10.014.
- Malamud, B. D., D. L. Turcotte, F. Guzzetti, and P. Reichenbach (2004), Landslides, earthquakes, and erosion, *Earth Planet. Sci. Lett.*, *229*(1–2), 45–59, doi:10.1016/j.epsl.2004.10.018.
- Marc, O., and N. Hovius (2015), Amalgamation in landslide maps: Effects and automatic detection, *Nat. Hazards Earth Syst. Sci.*, *15*(4), 723–733, doi:10.5194/nhess-15-723-2015.
- Marc, O., N. Hovius, P. Meunier, T. Uchida, and S. Hayashi (2015), Transient changes of landslide rates after earthquakes, *Geology*, *43*(10), 883–886, doi:10.1130/g36961.1.
- McPhillips, D., P. R. Bierman, and D. H. Rood (2014), Millennial-scale record of landslides in the Andes consistent with earthquake trigger, *Nat. Geosci.*, *7*(12), 925–930, doi:10.1038/ngeo2278.
- Meade, B. J. (2007), Present-day kinematics at the India-Asia collision zone, *Geology*, *35*(1), 81–84, doi:10.1130/g22924a.1.
- Meng, X.-L., R. Rosenthal, and D. B. Rubin (1992), Comparing correlated correlation coefficients, *Psychol. Bull.*, *111*(1), 172–175, doi:10.1037/0033-2909.111.1.172.
- Meunier, P., N. Hovius, and A. J. Haines (2007), Regional patterns of earthquake-triggered landslides and their relation to ground motion, *Geophys. Res. Lett.*, *34*, L20408, doi:10.1029/2007GL031337.
- Meunier, P., N. Hovius, and A. J. Haines (2008), Topographic site effects and the location of earthquake induced landslides, *Earth Planet. Sci. Lett.*, *275*(3–4), 221–232, doi:10.1016/j.epsl.2008.07.020.
- Moglen, G. E., E. A. B. Eltahir, and R. L. Bras (1998), On the sensitivity of drainage density to climate change, *Water Resour. Res.*, *34*(4), 855–862, doi:10.1029/97WR02709.
- Montgomery, D. R. (2001), Slope distributions, threshold hillslopes, and steady-state topography, *Am. J. Sci.*, *301*(4–5), 432–454, doi:10.2475/ajs.301.4-5.432.
- Montgomery, D. R., and M. T. Brandon (2002), Topographic controls on erosion rates in tectonically active mountain ranges, *Earth Planet. Sci. Lett.*, *201*(3–4), 481–489, doi:10.1016/S0012-821X(02)00725-2.
- Montgomery, D. R., and J. M. Buffington (1997), Channel-reach morphology in mountain drainage basins, *Geol. Soc. Am. Bull.*, *109*(5), 596–611, doi:10.1130/0016-7606(1997)109<0596:crmimd>2.3.co;2.
- Montgomery, D. R., and E. Foufoula-Georgiou (1993), Channel network source representation using digital elevation models, *Water Resour. Res.*, *29*(12), 3925–3934, doi:10.1029/93WR02463.
- Oglesby, D. D., and S. M. Day (2002), Stochastic fault stress: Implications for fault dynamics and ground motion, *Bull. Seismol. Soc. Am.*, *92*(8), 3006–3021, doi:10.1785/0120010249.
- Quimet, W. B., K. X. Whipple, and D. E. Granger (2009), Beyond threshold hillslopes: Channel adjustment to base-level fall in tectonically active mountain ranges, *Geology*, *37*(7), 579–582, doi:10.1130/G30013a.1.
- Parker, R. N., A. L. Densmore, N. J. Rosser, M. de Michele, Y. Li, R. Q. Huang, S. Whadcoat, and D. N. Petley (2011), Mass wasting triggered by the 2008 Wenchuan earthquake is greater than orogenic growth, *Nat. Geosci.*, *4*(7), 449–452, doi:10.1038/Ngeo1154.
- Pearce, A. J., and A. J. Watson (1986), Effects of earthquake-induced landslides on sediment budget and transport over a 50-yr period, *Geology*, *14*(1), 52–55, doi:10.1130/0091-7613(1986)14<52:eoelos>2.0.co;2.
- Ramos Scharón, C. E., E. J. Castellanos, and C. Restrepo (2012), The transfer of modern organic carbon by landslide activity in tropical montane ecosystems, *J. Geophys. Res.*, *117*, G03016, doi:10.1029/2011JG001838.
- Shen, Z. K., J. B. Sun, P. Z. Zhang, Y. G. Wan, M. Wang, R. Burgmann, Y. H. Zeng, W. J. Gan, H. Liao, and Q. L. Wang (2009), Slip maxima at fault junctions and rupturing of barriers during the 2008 Wenchuan earthquake, *Nat. Geosci.*, *2*(10), 718–724, doi:10.1038/ngeo636.
- Sklar, L., and W. E. Dietrich (1998), River Longitudinal Profiles and Bedrock Incision Models: Stream Power and the Influence of Sediment Supply, in *Rivers Over Rock: Fluvial Processes in Bedrock Channels*, edited by K. J. Tinkler and E. E. Wohl, AGU, Washington, D. C., doi:10.1029/GM107p0237.
- Stock, J., and W. E. Dietrich (2003), Valley incision by debris flows: Evidence of a topographic signature, *Water Resour. Res.*, *39*(4), 1089, doi:10.1029/2001WR001057.
- Sutherland, D. G., M. H. Ball, S. J. Hilton, and T. E. Lisle (2002), Evolution of a landslide-induced sediment wave in the Navarro River, California, *Geol. Soc. Am. Bull.*, *114*(8), 1036–1048, doi:10.1130/0016-7606(2002)114<1036:eoalis>2.0.co;2.
- Tang, C., J. Zhu, X. Qi, and J. Ding (2011), Landslides induced by the Wenchuan earthquake and the subsequent strong rainfall event: A case study in the Beichuan area of China, *Eng. Geol.*, *122*(1–2), 22–33, doi:10.1016/j.enggeo.2011.03.013.
- Tsai, Z.-X., G. J. Y. You, H.-Y. Lee, and Y.-J. Chiu (2013), Modeling the sediment yield from landslides in the Shihmen Reservoir watershed, Taiwan, *Earth Surf. Processes Landforms*, *38*(7), 661–674, doi:10.1002/esp.3309.
- Tucker, G. E., and R. L. Bras (1998), Hillslope processes, drainage density, and landscape morphology, *Water Resour. Res.*, *34*(10), 2751–2764, doi:10.1029/98WR01474.
- USGS Earthquake Hazard Program (2008), 06:28:01 UTC. [Available at <http://earthquake.usgs.gov/earthquakes/>]
- Wang, E., and Q. Meng (2009), Mesozoic and Cenozoic tectonic evolution of the Longmen Shan fault belt, *Sci. China Ser. D: Earth Sci.*, *52*(5), 579–592, doi:10.1007/s11430-009-0053-8.
- Wang, J., Z. Jin, R. G. Hilton, F. Zhang, A. L. Densmore, G. Li, and A. J. West (2015), Controls on fluvial evacuation of sediment from earthquake-triggered landslides, *Geology*, *43*(2), 115–118, doi:10.1130/g36157.1.
- West, A. J., C. W. Lin, T. C. Lin, R. G. Hilton, S. H. Liu, C. T. Chang, K. C. Lin, A. Galy, R. B. Sparkes, and N. Hovius (2011), Mobilization and transport of coarse woody debris to the oceans triggered by an extreme tropical storm, *Limnol. Oceanogr.*, *56*(1), 77–85, doi:10.4319/lo.2011.56.1.0077.

- West, A. J., R. Hetzel, G. Li, Z. Jin, F. Zhang, R. G. Hilton, and A. L. Densmore (2014), Dilution of ^{10}Be in detrital quartz by earthquake-induced landslides: Implications for determining denudation rates and potential to provide insights into landslide sediment dynamics, *Earth Planet. Sci. Lett.*, *396*, 143–153, doi:10.1016/j.epsl.2014.03.058.
- Whadcoat, S. K. (2011), Landsliding and sediment dynamics following the 2008 Wenchuan earthquake in the Beichuan area of China, Masters thesis, Durham Univ., Durham, England. [Durham E-Theses Online: Available at <http://etheses.dur.ac.uk/1369/>.]
- Xu, X., X. Wen, G. Yu, G. Chen, Y. Klinger, J. Hubbard, and J. Shaw (2009), Coseismic reverse- and oblique-slip surface faulting generated by the 2008 M_w 7.9 Wenchuan earthquake, China, *Geology*, *37*(6), 515–518, doi:10.1130/g25462a.1.
- Yanites, B. J., G. E. Tucker, K. J. Mueller, and Y. G. Chen (2010), How rivers react to large earthquakes: Evidence from central Taiwan, *Geology*, *38*(7), 639–642, doi:10.1130/G30883.1.
- Yuan, R. M., Q. H. Deng, D. Cunningham, C. Xu, X. W. Xu, and C. P. Chang (2013), Density distribution of landslides triggered by the 2008 Wenchuan earthquake and their relationships to peak ground acceleration, *Bull. Seismol. Soc. Am.*, *103*(4), 2344–2355, doi:10.1785/0120110233.
- Zhang, P. Z., et al. (2004), Continuous deformation of the Tibetan Plateau from Global Positioning System data, *Geology*, *32*(9), 809–812, doi:10.1130/g20554.1.
- Zhang, S., L. M. Zhang, and T. Glade (2014), Characteristics of earthquake- and rain-induced landslides near the epicenter of Wenchuan earthquake, *Eng. Geol.*, *175*, 58–73, doi:10.1016/j.enggeo.2014.03.012.